

Learned Finite Element-based Regularization of the Inverse Problem in Electrocardiographic Imaging

Manuel Haas[†]

Thomas Grandits[‡]

Thomas Pinetz[§]

Thomas Beiert[¶]

Simone Pezzuto^{||}

Alexander Effland[†]

February 10, 2026

Abstract

Electrocardiographic imaging (ECGI) seeks to reconstruct cardiac electrical activity from body-surface potentials noninvasively. However, the associated inverse problem is severely ill-posed and requires robust regularization. While classical approaches primarily employ spatial smoothing, the temporal structure of cardiac dynamics remains underexploited despite its physiological relevance. We introduce a space–time regularization framework that couples spatial regularization with a learned temporal Fields-of-Experts (FoE) prior to capture complex spatiotemporal activation patterns. We derive a finite element discretization on unstructured cardiac surface meshes, prove Mosco-convergence, and develop a scalable optimization algorithm capable of handling the FoE term. Numerical experiments on synthetic epicardial data demonstrate improved denoising and inverse reconstructions compared to handcrafted spatiotemporal methods, yielding solutions that are both robust to noise and physiologically plausible.

1 Introduction

The heart is an electromechanical pump essential to sustaining life. Abnormal electrical activation may lead to life-threatening arrhythmias, which must be promptly diagnosed to prevent further damage. In electrocardiography, electrical potentials recorded on the chest surface are linked to the underlying cardiac electrical activity and can therefore provide insight into arrhythmic mechanisms and guide therapeutic decisions [24]. From a mathematical perspective, reconstructing cardiac potentials from body-surface measurements leads to the inverse problem of electrocardiography [5, 6]. This inverse problem is severely ill-posed, and its difficulty is further exacerbated by noise and measurement artifacts arising from imperfect electrode contact and anatomical constraints [1]. Consequently, the choice of regularization is critical for obtaining physiologically meaningful reconstructions.

https://github.com/mnlhaas/ECGI_FEM

*This work was supported by the Deutsche Forschungsgemeinschaft (DFG, German Research Foundation), EXC2151-390873048, EXC-2047/1-390685813, and – CRC 1720 – 539309657. SP and TG are also supported by the SNSF project “CardioTwin” (no. 214817). SP acknowledges the support of the CSCS-Swiss National Supercomputing Centre project no. lp100 and the PRIN-PNRR project no. P2022N5ZNP. SP is member of INdAM-GNCS.

[†]Institute of Applied Mathematics, University of Bonn, Germany

[‡]Institute of Artificial Intelligence, Medical University of Vienna, Austria

[§]Euler Institute, Università della svizzera italiana, Switzerland; Department of Mathematics and Scientific Computing, University of Graz, Austria

[¶]Heart Center Bonn, Department of Internal Medicine II, University Hospital Bonn, Germany

^{||}Department of Mathematics, University of Trento, Italy

A broad range of regularization techniques has been investigated to stabilize the reconstructions [17], ranging from classical Tikhonov methods [31] to total variation [28] approaches. While spatial regularization has been widely studied, the temporal dimension in medical imaging remains underutilized, despite its importance for capturing complex spatiotemporal activation patterns, such as the wave-like propagation observed in cardiac electrical potentials [15, 22]. Deep learning techniques demonstrate good accuracy in inverse problem reconstruction [30], and optimization-based approaches in machine learning frameworks have been explored for patient-specific cardiac modeling [14], but provide limited interpretability.

Recently, machine-learned priors such as Fields-of-Experts (FoE) [7, 13, 27] and variational deep regularizers [18] have demonstrated strong performance in modeling higher-order dependencies in image reconstruction tasks and retain interpretability, yet their integration with PDE-constrained inverse problems in finite element frameworks remains largely unexplored. In this work, we propose a novel class of learned finite element regularizers that combine spatial total variation-type terms with a data-driven temporal FoE prior. Both the cardiac inverse problem and the proposed regularization are discretized within a finite element framework [3, 4, 29, 32].

Beyond modeling, our main theoretical contribution is the first Mosco-convergence analysis for inverse problems regularized by learned FoE-type energies in finite element spaces, proving convergence of minimizers from the discrete to the continuous problem on realistic domains [8, 20, 21]. Numerical experiments demonstrate that the proposed learning-analysis framework produces reconstructions that are both more accurate and more physiologically plausible than those obtained by classical non-learning-based methods. The paper is structured as follows: we first introduce a variational model with learned spatiotemporal regularization, then present its finite element discretization on unstructured cardiac meshes, establish Mosco-convergence and convergence of minimizers, develop a scalable convergent optimization algorithm, and finally validate the approach with numerical experiments on synthetic 2D data.

2 Methods

We begin by introducing the forward and inverse problems in electrocardiographic imaging (ECGI), along with the FoE-based regularization.

2.1 Forward Problem

The forward problem consists of computing body-surface potentials resulting from a given epicardial potential, obtained by transferring the epicardial potential through the torso volume conductor via a linear forward operator. Let $\Omega \subset \mathbb{R}^d$ with $d \in \{2, 3\}$ denote the torso domain with outer boundary $\Gamma = \partial\Omega$. The body-surface electrodes are represented by a subset $\Sigma \subset \Gamma$, consisting of a disjoint union of N_Σ open and bounded patches $\Sigma = \bigcup_{i=1}^{N_\Sigma} \Sigma_i$ for each electrode, where measurements z are available. The epicardial surface of the heart is denoted by $\Gamma_H = \partial\Omega_H$, where $\Omega_H \subset \Omega$ is the heart domain. We define the torso domain excluding the heart as $\Omega_0 = \Omega \setminus \overline{\Omega}_H$. Throughout, we assume that the domain Ω_0 possesses a C^2 boundary, and that both Γ_H and Γ are closed and compact disjunct boundary manifolds. For a time interval $\mathbb{T} := (0, \tilde{t})$ with $\tilde{t} > 0$ and the epicardium potential function $u \in L^2(\mathbb{T}; H^{1/2}(\Gamma_H))$, the well-posed elliptic forward problem is defined for almost every $t \in \mathbb{T}$

$$\begin{cases} -\operatorname{div}(\sigma(\mathbf{x})\nabla_{\mathbf{x}}v(\mathbf{x}, t)) = 0, & \mathbf{x} \in \Omega_0, \\ \sigma(\mathbf{x})\nabla_{\mathbf{x}}v(\mathbf{x}, t) \cdot \mathbf{n} = 0, & \mathbf{x} \in \Gamma, \\ v(\mathbf{x}, t) = u(\mathbf{x}, t), & \mathbf{x} \in \Gamma_H, \end{cases} \quad (1)$$

for \mathbf{n} the outward unit normal vector and $\sigma \in L^\infty(\Omega, \mathbb{R}_+)$ the torso conductivity tensor or bulk conductivity. Here, we assume the space-dependent matrix σ to be symmetric

satisfying the ellipticity condition $\zeta^{-1}|\mathbf{y}|^2 \leq \sigma(\mathbf{x})\mathbf{y} \cdot \mathbf{y} \leq \zeta|\mathbf{y}|^2$ for some $\zeta > 0$ and all $\mathbf{y} \in \mathbb{R}^d$. The existence, uniqueness, and regularity of a solution follow [10].

Theorem 1. *There exists a unique solution $v \in L^2(\mathbb{T}; H^1(\Omega_0))$ of (1) for $u \in L^2(\mathbb{T}; H^{1/2}(\Gamma_H))$ in a weak sense.*

Proof. For a.e. $t \in \mathbb{T}$, the surjectivity of the trace operator from $H^1(\Omega_0)$ to $H^{1/2}(\Gamma_H)$ yields a function $g(\cdot, t) \in H^1(\Omega_0)$ with $g|_{\Gamma_H} = u(\cdot, t)$ and

$$\|g(\cdot, t)\|_{H^1(\Omega_0)} \leq C_E \|u(\cdot, t)\|_{H^{1/2}(\Gamma_H)}.$$

Writing $v(\cdot, t) = g(\cdot, t) + w(\cdot, t)$ with $w(\cdot, t) \in H_0^1(\Omega_0)$ reduces (1) to homogeneous boundary conditions. Defining $a(\phi, \varphi) := \int_{\Omega_0} \sigma \nabla_{\mathbf{x}} \phi \cdot \nabla_{\mathbf{x}} \varphi \, d\mathbf{x}$ with $\phi, \varphi \in H_0^1(\Omega_0)$, which is continuous and coercive, the Lax–Milgram theorem gives for a.e. $t \in \mathbb{T}$ a unique $w(\cdot, t) \in H_0^1(\Omega_0)$ solving

$$a(w(\cdot, t), \varphi) = -a(g(\cdot, t), \varphi) \quad \forall \varphi \in H_0^1(\Omega_0), \quad (2)$$

with $\|w(\cdot, t)\|_{H^1(\Omega_0)} \leq C \|g(\cdot, t)\|_{H^1(\Omega_0)}$. Hence $v(\cdot, t)$ satisfies the weak formulation of (1) and $\|v(\cdot, t)\|_{H^1(\Omega_0)} \leq C \|u(\cdot, t)\|_{H^{1/2}(\Gamma_H)}$. Integration over \mathbb{T} yields the claim, and uniqueness follows from coercivity. \square

Let $v_u(\cdot, t)$ be the weak solution associated with the boundary data $u(\cdot, t)$ for a.e. $t \in \mathbb{T}$. We define the operator

$$A_{\mathbb{T}} : H^{1/2}(\Gamma_H) \rightarrow H^{1/2}(\Gamma), \quad \text{with} \quad A_{\mathbb{T}}[u(\cdot, t)] := v_u(\cdot, t)|_{\Gamma}$$

as the solution operator concatenated with the trace operator for the torso boundary. Therefore, the forward operator is a bounded linear operator, and since $u(\cdot, t) : \mathbb{T} \rightarrow H^{1/2}(\Gamma_H)$ is strongly measurable, the composition $A_{\mathbb{T}}[u(\cdot, t)]$ is strongly measurable (because $H^{1/2}(\Gamma)$ is separable), ensuring boundedness by

$$\|A_{\mathbb{T}}[u(\cdot, t)]\|_{H^{1/2}(\Gamma)} \leq C \|v(\cdot, t)\|_{H^1(\Omega_0)} \leq \tilde{C} \|u(\cdot, t)\|_{H^{1/2}(\Gamma_H)}.$$

By integrating over time, we define the linear forward operator

$$A : L^2(\mathbb{T}; H^{1/2}(\Gamma_H)) \rightarrow L^2(\mathbb{T}; H^{1/2}(\Gamma)), \quad u \mapsto v_u|_{\Gamma}.$$

Note that the inverse of the forward operator is, in general, unbounded.

2.2 Inverse Problem

For the inverse problem in electrocardiography, we compare to a time series of measurements $z \in (L^2(\mathbb{T}))^{N_{\Sigma}}$ for each electrode $i = 1, \dots, N_{\Sigma}$ defined by the average integral $z_i(t) = \int_{\Sigma_i} \tilde{z}(\mathbf{x}, t) dS^{\Gamma}(\mathbf{x})$ of a potential function $\tilde{z} \in L^2(\Sigma \times \mathbb{T})$ with the $d-1$ -dimensional surface measure S^{Γ} of Γ . Since the measurements are defined electrode-wise as scalars, we minimize the cost functional

$$\arg \min_{u \in L^2(\mathbb{T}; H^{1/2}(\Gamma_H))} \left\{ G(u, z) := \frac{1}{2N_{\Sigma}} \sum_{i=1}^{N_{\Sigma}} \int_{\mathbb{T}} \left(\int_{\Sigma_i} A[u](\mathbf{x}, t) dS^{\Gamma}(\mathbf{x}) - z_i(t) \right)^2 dt \right\}.$$

Due to the ill-posedness of the problem, we follow the standard approach in inverse problem theory and introduce a regularization term. The inverse problem is formulated as the minimization of an energy functional consisting of a data fidelity term and a regularization term. For a given measurement $z \in (L^2(\mathbb{T}))^{N_{\Sigma}}$, we seek an epicardial potential u that minimizes

$$\arg \min_{u \in \mathcal{V}} \{ \mathcal{J}(u, z) := G(u, z) + R_{\theta}(u) \}, \quad (3)$$

over the space $\mathcal{V} := L^2(\mathbb{T}; H^1(\Gamma_H))$. The choice of \mathcal{V} as space of solutions follows from the continuous embedding $H^1(\Gamma_H) \hookrightarrow H^{1/2}(\Gamma_H)$ on compact C^2 manifolds, hence $\mathcal{V} \subset L^2(\mathbb{T}; H^{1/2}(\Gamma_H))$. The norm of the Bochner space \mathcal{V} is defined as

$$\|u\|_{\mathcal{V}} = \left(\int_{\mathbb{T}} \|u(\cdot, t)\|_{H^1(\Gamma_H)}^2 dt \right)^{\frac{1}{2}} = \left(\int_{\Gamma_H \times \mathbb{T}} (u(\mathbf{x}, t))^2 + |\nabla_{\Gamma_H} u(\mathbf{x}, t)|^2 d\Pi(\mathbf{x}, t) \right)^{\frac{1}{2}}$$

with surface gradient ∇_{Γ_H} for any $v : \Gamma_H \rightarrow \mathbb{R}$ and $d\Pi(\mathbf{x}, t) := dS(\mathbf{x}) \otimes d\lambda(t)$ with S the $(d-1)$ -dimensional surface measure of Γ_H and λ the 1-dimensional Lebesgue measure. Moreover, we define the space $\mathcal{Y} := L^2(\Gamma_H \times \mathbb{T})$ to allow for more convenient notation of norms.

2.3 Spatiotemporal Regularizer

Standard regularization techniques such as Tikhonov [31] and total variation [28] are general-purpose approaches that effectively mitigate measurement noise. Here, we aim to design a problem-specific regularizer that embeds data-driven knowledge of the underlying cardiac dynamics while remaining mathematically well-posed and interpretable.

To this end, we adopt the FoE framework, originally developed for imaging, in which, instead of prescribing a fixed penalty, one learns a collection of experts [7, 13, 27]. Each expert $i = 1, \dots, N_C$ is defined by a bounded linear operator L_i acting on the epicardial potential and an associated nonlinear potential function ϕ_i . The operator response $L_i[u]$ is penalized pointwise in space and time via ϕ_i . Overall, the regularizer in a continuous spatiotemporal formulation reads as

$$R_{\theta}(u) = \sum_{i=1}^{N_C} \int_{\Gamma_H \times \mathbb{T}} \phi_i(L_i[u](\mathbf{x}, t)) d\Pi(\mathbf{x}, t). \quad (4)$$

In canonical FoE, the operators L_i are chosen as convolutions with learned kernels, mirroring convolutional layers in neural networks. However, spatiotemporal convolutions on unstructured finite element grids are computationally expensive due to their irregular structure, whereas temporal convolutions on a typically uniform time grid are straightforward to compute. We therefore propose a multivariate operator that separates spatial differentiation from temporal filtering while still allowing joint, learned coupling of their responses. In our formulation, the operators L_i consist of three components: a zero-order term $\epsilon_{\theta} u$ ensuring stability, the surface gradient $\nabla_{\Gamma_H} u$ imposing spatial regularity, and a temporally filtered component $K_i[u]$ such that

$$L_i[u](\mathbf{x}, t) \in \mathbb{R} \times \mathbb{R}^d \times \mathbb{R} \quad \text{with} \quad L_i[u] := (\epsilon_{\theta} u, \nabla_{\Gamma_H} u, K_i[u]), \quad (5)$$

where $\epsilon_{\theta} > 0$ is a learned scalar and K_i is realised as a bounded temporal cross correlation with a 1D kernel $k_i \in L^1(\widetilde{\mathbb{T}})$ with $\widetilde{\mathbb{T}} = (-\omega/2, \omega/2)$ for $\omega > 0$ applied to the zero-extended signal \tilde{u}

$$K_i[u] := (k_i *_{\mathbb{T}} u)(\mathbf{x}, t) := \mathbf{1}_{\mathbb{T}}(t) \int_{\widetilde{\mathbb{T}}} k_i(\tau) \tilde{u}(\mathbf{x}, \tau + t) d\tau, \quad \tilde{u} = u \text{ on } \mathbb{T}, \quad \tilde{u} = 0 \text{ otherwise.}$$

We adapt the multivariate setting introduced in [7] such that the corresponding potentials $\phi_i : \mathbb{R}^{d+2} \rightarrow \mathbb{R}$ penalize the joint response of the components in (5). Hence, (4) becomes

$$R_{\theta}(u) = \lambda_{\theta} \sum_{i=1}^{N_C} \int_{\Gamma_H \times \mathbb{T}} \phi_i(\epsilon_{\theta} u(\mathbf{x}, t), \nabla_{\Gamma_H} u(\mathbf{x}, t), (k_i *_{\mathbb{T}} u)(\mathbf{x}, t)) d\Pi(\mathbf{x}, t), \quad (6)$$

with weighting parameter $\lambda_{\theta} > 0$. The filters k_i and parameters of ϕ_i are learned from data, jointly with ϵ_{θ} and λ_{θ} ; the spatial operator ∇_{Γ_H} is fixed by the geometry.

Following [7], to construct flexible and well-behaved multivariate potentials, we rely on the concept of the Moreau envelope [19]. Given a proper, lower semi-continuous, convex function $f : \mathbb{R}^{d+2} \rightarrow \mathbb{R}$ and a parameter $\mu > 0$, its Moreau envelope is defined as $M_\mu f(\mathbf{x}) = \inf_{\mathbf{z} \in \mathbb{R}^{d+2}} \left\{ f(\mathbf{z}) + \frac{1}{2\mu} \|\mathbf{z} - \mathbf{x}\|_2^2 \right\}$. The Moreau envelope can be viewed as a smooth approximation of f that preserves key properties of the original function while ensuring differentiability and well-behaved gradients. In particular, its gradient is directly related to the proximal operator of f , $\nabla M_\mu f(\mathbf{x}) = \frac{1}{\mu} (\mathbf{x} - \text{prox}_{\mu f}(\mathbf{x}))$, which is non-expansive, implying Lipschitz continuity of $\nabla M_\mu f$, and computationally efficient to evaluate for many choices of f . These properties make the Moreau envelope particularly suitable for designing potentials in optimization-based inverse problems, where stable and efficient gradient computation is crucial. Building on this idea, we define our multivariate potential functions as differences of Moreau envelopes of the ℓ^∞ norm, combined with linear transformations and a zero-order Tikhonov term. For each operator L_i , the potential function is

$$\phi_i(\mathbf{y}) = \mu_i \omega_{\mu_i}^{d+2}(\mathbf{y}) - \mu_i \omega_{\eta_i \mu_i}^{d+2}(\mathbf{Q}_i \mathbf{y}), \quad (7)$$

with learnable matrices $\mathbf{Q}_i \in \mathbb{R}^{(d+2) \times (d+2)}$ and scalars η_i , where

$$\omega_\mu^{d+2}(\mathbf{y}) = \left\| \mathbf{y} - \mu \text{Proj}_{B_{\ell^1}}(\mathbf{y}/\mu) \right\|_\infty + \frac{\mu}{2} \left\| \text{Proj}_{B_{\ell^1}}(\mathbf{y}/\mu) \right\|_2^2 + \frac{\epsilon_\omega}{2} \|\mathbf{y}/\mu\|_2^2,$$

and $\text{prox}_{\iota_{B_{\ell^1}}}(\mathbf{y}) = \text{Proj}_{B_{\ell^1}}(\mathbf{y}) = \arg \min_{\mathbf{z} \in B_{\ell^1}} \{\|\mathbf{z} - \mathbf{y}\|_2^2\}$, the projection onto the ℓ^1 -ball in \mathbb{R}^{d+2} for indicator function of the ℓ^1 -ball $\iota_{B_{\ell^1}}$. This construction ensures several desirable properties: it favors weak responses while increasingly penalizing strong ones, captures correlations across multiple components via \mathbf{Q}_i , and remains smooth and coercive due to the Moreau envelope and zero-order term. The derivative of ω_μ^{d+2} , $\nabla \omega_\mu^{d+2}(\mathbf{y}) = \text{Proj}_{B_{\ell^1}}(\mathbf{y}/\mu) + \epsilon_\omega \mathbf{y}/\mu$, is computationally efficient and non-expansive, ensuring stability in gradient-based optimization.

According to [7, Theorem 1], the conditions $\|\mathbf{Q}_i\|_\infty \leq 1$ and $\eta_i > \|\mathbf{Q}_i\|_2^2$ guarantee that the potential ϕ_i is nonnegative and attains a unique global minimum at the origin, which carries over naturally to our framework and ensures that the learned regularizer is bounded from below while favoring weak operator responses. We also note that the regularization functional R_θ is differentiable, allowing for efficient gradient-based optimization. However, due to the negative part in (7), it is generally non-convex, reflecting the trade-off between expressivity and convexity.

3 Finite Element Discretization

In this section, we introduce the discrete domains, function spaces, and operators used throughout this work, constructed via the finite element method (FEM).

3.1 Space-Time Discretization

We define \mathcal{T}_h with largest element diameter $h > 0$ as the collection of surface elements discretizing Γ_H and, with a slight misuse of notation, the shape-regular adaptive conforming surface mesh approximating Γ_H . Furthermore, we assume that the elements in \mathcal{T}_h are restricted to vertices lying on Γ_H . Analogously, we discretize Γ and consistent as subsets Σ_i by \mathcal{T}_h^Γ and $\mathcal{T}_h^{\Sigma_i}$ for $i = 1, \dots, N_\Sigma$. The torso domain Ω_0 is discretized by a mesh \mathcal{U}_h , which is defined as a shape-regular volumetric discretization satisfying $\mathcal{T}_h \cup \mathcal{T}_h^\Gamma = \partial \mathcal{U}_h$ either consisting of triangles ($d = 2$) or tetrahedra ($d = 3$).

The temporal interval \mathbb{T} is discretized as a uniform temporal grid \mathcal{S}_h . In particular, we assume that temporal measurements are available at $N_{\mathbb{T}} + 1$ equidistant time points $t_s = s\delta$ for $s = 0, \dots, N_{\mathbb{T}}$ which define $N_{\mathbb{T}}$ time intervals of size $\delta > 0$, with $\delta = O(h)$.

3.2 Function Spaces

We approximate the continuous space-time function space \mathcal{V} by the discrete space \mathcal{V}_h using P_1 finite elements in space on the adaptive surface mesh \mathcal{T}_h and in time on the temporal grid \mathcal{S}_h . The spatial mesh is identical at each time step and consists of affine elements of dimension d . Let $\Xi := \{\xi_i\}_{i=1}^{N_V} \subset \Gamma_H$ denote the set of nodes associated with \mathcal{T}_h . The tensor product of a spatial element $J \in \mathcal{T}_h$ and a temporal interval $Z \in \mathcal{S}_h$ defines a space-time element $J \otimes Z \in \mathcal{T}_h \otimes \mathcal{S}_h$. The resulting discrete space-time function space is

$$\mathcal{V}_h := \left\{ v \in L^2(\mathbb{T}; H^1(\mathcal{T}_h)) : v|_{J \otimes Z} \in P_1(J) \otimes P_1(Z), \forall J \in \mathcal{T}_h, Z \in \mathcal{S}_h \right\},$$

with spatial and temporal basis functions $\{\varphi_i\}_{i=1}^{N_V}$ and $\{\rho_s\}_{s=0}^{N_T}$, respectively. Any discrete function $u_h \in \mathcal{V}_h$ can be expressed as

$$u_h(\mathbf{x}, t) = \sum_{s=0}^{N_T} \sum_{i=1}^{N_V} \mathbf{u}_{i,s} \varphi_i(\mathbf{x}) \rho_s(t),$$

where $\mathbf{u}_{i,s}$ is the value at node (ξ_i, t_s) with $\mathbf{u} = (\mathbf{u}_{1,0}, \mathbf{u}_{2,0}, \dots, \mathbf{u}_{N_V, N_T}) \in \mathbb{R}^{N_V \times (N_T+1)}$. Next, we examine the function spaces induced by the linear operators L_i . Since P_1 functions are affine on each mesh element $T \in \mathcal{T}_h$, their spatial gradients are element-wise constant and belong to the broken L^2 space

$$P_0(\mathcal{T}_h) := \{v \in L^2(\Omega) : v|_T \text{ is constant for all } T \in \mathcal{T}_h\}.$$

This defines a discrete gradient space \mathcal{Q}_h composed of vector-valued functions $p_h = (p_{h_1}, \dots, p_{h_d})^\top$ with $p_{h_k} \in L^2(\mathcal{T}_h \times \mathbb{T})$ for $k = 1, \dots, d$, that are piecewise constant in space per element and affine in time:

$$\mathcal{Q}_h := \left\{ p \in (L^2(\mathcal{T}_h \times \mathbb{T}))^d : p_k|_{J \otimes Z} \in P_0(J) \otimes P_1(Z), \forall J \in \mathcal{T}_h, Z \in \mathcal{S}_h \right\}.$$

Here, $\{\vartheta_l\}_{l=1}^{N_Q}$ denotes the basis of $P_0(\mathcal{T}_h)$ with $N_Q \in \mathbb{N}$. The temporal cross-correlation in the regularizer function acts on functions $u_h \in \mathcal{V}_h$ as $k_h *_{\mathbb{T}} \cdot : \mathcal{V}_h \rightarrow \mathcal{W}_h$, where the cross-correlation of piecewise affine functions yields a piecewise cubic one

$$\mathcal{W}_h := \left\{ w \in L^2(\mathbb{T}; H^1(\mathcal{T}_h)) : w|_{J \otimes Z} \in P_1(J) \otimes P_3(Z), \forall J \in \mathcal{T}_h, Z \in \mathcal{S}_h \right\}.$$

We approximate time-dependent functions using the standard piecewise linear hat functions ρ_i on the uniform temporal grid t_0, \dots, t_{N_T} with step size δ , defined by $\rho_i(t) = \max\{0, 1 - |t - t_i|/\delta\}$ for $i = 0, \dots, N_T$. These functions naturally lead to the temporal mass matrix

$$\tilde{\mathbf{D}}_{ij} = \int_{\mathbb{T}} \rho_i(t) \rho_j(t) dt = \frac{\delta}{6} \begin{cases} 4, & i = j, 1 \leq i \leq N_T - 1, \\ 2, & i = j, i \in \{0, N_T\}, \\ 1, & |i - j| = 1, \\ 0, & \text{otherwise.} \end{cases}$$

In space, we employ piecewise affine basis functions φ_i on the mesh \mathcal{T}_h , leading to the spatial mass matrix

$$\tilde{\mathbf{M}}_{ij} = \int_{\mathcal{T}_h} \varphi_i(\mathbf{x}) \varphi_j(\mathbf{x}) d\mathbf{x}, \quad 1 \leq i, j \leq N_V.$$

To handle functions that depend on both space and time, we combine the temporal and spatial matrices using tensor products $\tilde{\mathbf{D}} = \mathbf{D} \otimes \mathbf{I}_{N_V}$ and $\tilde{\mathbf{M}} = \mathbf{I}_{S+1} \otimes \mathbf{M}$. This

construction ensures that the resulting matrices correctly account for all degrees of freedom of the discrete solution $u_h \in \mathcal{V}_h$, linking each spatial node with every time step. Finally, for vector-valued functions with d components, we define the standard L^2 inner product on the space-time domain $\mathcal{T}_h \times \mathbb{T}$ by

$$(v_h, w_h)_{\mathcal{Y}_h^d} = \sum_{i=1}^d \int_{\mathcal{T}_h \times \mathbb{T}} v_{h,i}(\mathbf{x}, t) w_{h,i}(\mathbf{x}, t) d(\mathbf{x}, t),$$

where $\mathcal{Y}_h := L^2(\mathcal{T}_h \times \mathbb{T})$. This inner product provides the natural framework for measuring errors and formulating the fully discrete variational problem.

3.3 Forward Operator

The discretization of the forward operator A in piecewise affine finite elements follows [32]. For almost all $t \in \mathbb{T}$, we consider the discrete version of (2)

$$a_h(v_h(\cdot, t), \varphi_h) = \int_{\mathcal{U}_h} \sigma_h(\mathbf{x}) \nabla_{\mathbf{x}} v_h(\mathbf{x}, t) \cdot \nabla_{\mathbf{x}} \varphi_h(\mathbf{x}) d\mathbf{x} = 0 \quad \forall \varphi_h \in P_1(\mathcal{U}_h), \varphi_h|_{\mathcal{T}_h} = 0 \quad (8)$$

with boundary conditions on the epicardium given by $v_h|_{\mathcal{T}_h} = u_h$ for some $u_h \in \mathcal{V}_h$. Equivalently, we set $v_h = w_h + g_h$, where $w_h|_{\mathcal{T}_h} = 0$ and $g_h|_{\mathcal{T}_h} = u_h$, leading to

$$a_h(w_h(\cdot, t), \varphi_h) = -a_h(g_h(\cdot, t), \varphi_h) \quad \forall \varphi_h \in P_1(\mathcal{U}_h), \varphi_h|_{\mathcal{T}_h} = 0. \quad (9)$$

By coercivity and continuity of a , for fixed boundary data u_h , (8) admits a unique solution v_h . The discrete forward operator A_h is then defined by restricting v_h to the torso boundary, i.e. $A_h[u_h] = v_h|_{\Gamma}$. In practice, for each timestep $t \in \mathbb{T}$, this corresponds to solving a linear system for the piecewise affine finite element coefficients of v_h , yielding the mapping $\mathbf{v}_u = \mathbf{A}\mathbf{u}$ from epicardium potentials to torso boundary.

3.4 Linear Operators in the Regularizer

The regularization functional involves linear operators $L[u] = (\epsilon_{\theta} u, \nabla_{\Gamma_H} u, K[u])$. For the spatial gradient, we exploit the fact that piecewise affine functions on a manifold mesh admit the exact gradient representation

$$\|\nabla_{\Gamma_H}^h u_h\|_{\mathcal{Y}_h^d} = \|\nabla_{\Gamma_H} u_h\|_{\mathcal{Y}_h^d}$$

for $u_h \in \mathcal{V}_h$. The restriction $u_h|_J$ for $J \in \mathcal{T}_h$ with nodes $(\xi_i)_{i=1}^3$ is affine, and consequently, the elementwise constant Euclidean gradient can be written as

$$\nabla_{\Gamma_H} u_h|_J(\mathbf{x}) = \sum_{i=1}^3 u_h(\xi_i) \nabla_{\Gamma_H} \varphi_i(\mathbf{x}),$$

where $\{\varphi_i\}_{i=1}^3$ are the local nodal basis functions. The discrete gradient is defined by tangential projection, $\nabla_{\Gamma_H}^h u_h|_J := (\mathbf{I}_d - \mathbf{n}_J \otimes \mathbf{n}_J) \nabla_{\Gamma_H} u_h|_J$, where \mathbf{n}_J denotes the unit normal of J . We denote by ∇_{Γ_H} the matrix representation of $\nabla_{\Gamma_H}^h$ acting on the nodal values of piecewise affine functions. By approximating $k \in L^1(\mathbb{T})$ with piecewise affine temporal finite elements $k_h \in P_1(\tilde{\mathcal{S}}_h)$ for a discretization $\tilde{\mathcal{S}}_h$ using standard L^2 -projection, we obtain the discrete operator K_h and a nodal vector \mathbf{k} . The temporal kernel k_h is defined on an extended interval $\tilde{\mathbb{T}} = [t_{-N_w}, t_{N_w}]$ with $N_w \in \mathbb{N}$, while u_h is defined on \mathbb{T} . The temporal cross-correlation $K_h[u_h](\mathbf{x}, t) = (k_h *_{\mathbb{T}} u_h)(\mathbf{x}, t)$ is discretized as

$$K_h[u_h](\mathbf{x}, t) = \mathbf{1}_{\mathbb{T}}(t) \int_{\tilde{\mathbb{T}}} k_h(\tau) u_h(\mathbf{x}, \tau + t) d\tau = \sum_{i=1}^{N_V} \sum_{l=0}^{N_{\mathbb{T}}} \sum_{j=1}^{2N_w} \mathbf{u}_{i,l} \mathbf{k}_j \mathbf{D}_{lj}(t) \varphi_i(\mathbf{x}).$$

Let \mathbf{K} denote the matrix of K_h . The resulting discretized operator is

$$L_h : \mathcal{V}_h \rightarrow \mathcal{V}_h \times \mathcal{Q}_h \times \mathcal{W}_h, \quad L_h[u_h] := (\epsilon_\theta u_h, \nabla_{\Gamma_H}^h u_h, K_h[u_h]). \quad (10)$$

The projection onto the norm ball associated with the potential functions ϕ_i in (7) is a pointwise operation and therefore requires all involved discrete quantities to be represented in the same finite element space. However, the discrete operator L_h maps into a space of piecewise constant functions, which do not admit well-defined point values on element interfaces. As a consequence, the projection cannot be applied directly. We introduce an interpolation operator $\mathcal{P}_h : \mathcal{V}_h \times \mathcal{Q}_h \times \mathcal{W}_h \rightarrow (\mathcal{V}_h)^{d+2}$ such that $\tilde{L}_h = \mathcal{P}_h \circ L_h$. Note that the evaluation of the different dimensions in the linear operator in the same finite element space is not necessary for the squared ℓ^2 -norm part of ϕ_i . We define a variant $\tilde{\phi}_i$ of ϕ_i with $\tilde{\omega}_{\mu_i}^{d+2}$ such that

$$\tilde{\omega}_{\mu}^{d+2}(\mathbf{y}, \tilde{\mathbf{y}}) = \left\| \tilde{\mathbf{y}} - \mu \text{Proj}_{B_{\ell^1}}(\tilde{\mathbf{y}}/\mu) \right\|_{\infty} + \frac{\mu}{2} \left\| \text{Proj}_{B_{\ell^1}}(\tilde{\mathbf{y}}/\mu) \right\|_2^2 + \frac{\epsilon_\omega}{2} \|\mathbf{y}/\mu\|_2^2, \quad (11)$$

accounting for the difference in L_h and \tilde{L}_h . We start with defining the interpolation operator \mathcal{P}_h . The cross-correlation of two piecewise affine functions is piecewise cubic and globally continuous in the nodal basis. To this end, we evaluate the cross-correlation at the temporal nodes of \mathcal{V}_h and introduce an interpolation operator

$$\mathcal{P}_h^{\text{temp}} : C^0(\overline{\mathbb{T}}) \rightarrow P_1(\mathcal{S}_h), \quad \mathcal{P}_h^{\text{temp}}[u](t) = \sum_{s=0}^{N_{\mathbb{T}}} u(t_s) \rho_s(t),$$

with continuity for piecewise affine interpolations $\|\mathcal{P}_h^{\text{temp}}[v]\|_{L^2(\mathbb{T})} \leq C \|v\|_{L^2(\mathbb{T})}$ for $v \in C^0(\overline{\mathbb{T}})$. Remark that for any piecewise cubic function $v_h \in P_3(\mathcal{S}_h)$, we compute an upper bound [3] by the boundedness of the second derivative of v_h

$$\|\mathcal{P}_h^{\text{temp}} v_h - v_h\|_{L^2(\mathbb{T})} \leq Ch^2 \|\partial_{tt} v_h\|_{L^2(\mathbb{T})}. \quad (12)$$

We further define a spatial interpolation operator $\mathcal{P}_h^{\text{sp}} : L^2(\mathcal{T}_h) \rightarrow P_1(\mathcal{T}_h)$ as the L^2 -projection onto the subspace of piecewise affine spatial functions, allowing for computation of the piecewise affine projection of piecewise constant functions. The aforementioned L^2 -projection is defined by

$$\mathcal{P}_h^{\text{sp}}[p] = \arg \min_{p_h \in P_1(\mathcal{T}_h)} \{ \|p - p_h\|_{\mathcal{Y}_h} \}.$$

This orthogonal projection is computed by its optimality condition

$$\int_{\mathcal{T}_h} \tilde{p}_h(\mathbf{x}) \varphi(\mathbf{x}) d\mathbf{x} = \int_{\mathcal{T}_h} p_h(\mathbf{x}) \varphi(\mathbf{x}) d\mathbf{x}, \quad \forall \varphi \in P_1(\mathcal{T}_h) \quad (13)$$

with $\tilde{p}_h := \mathcal{P}_h^{\text{sp}}[p_h]$. By choosing φ as the basis functions $(\varphi_i)_{i=1}^{N_{\mathcal{V}}}$ and $p_h \in P_0(\mathcal{T}_h)$, we compute the nodal values $\tilde{\mathbf{p}}$ of the projection by

$$\tilde{\mathbf{M}} \tilde{\mathbf{p}} = \mathbf{b} \quad \text{with} \quad \mathbf{b}_i = \int_{\mathcal{T}_h} p_h(\mathbf{x}) \varphi_i(\mathbf{x}) d\mathbf{x} = \sum_{j: \xi_i \in J_j} \mathbf{p}_j \int_{J_j} \varphi_i(\mathbf{x}) d\mathbf{x} = \sum_{j: \xi_i \in J_j} \mathbf{p}_j \frac{|J_j|}{d}$$

with φ_i the basis function associated with node ξ_i for $i = 1, \dots, N_{\mathcal{V}}$. We define the matrix representations of $\mathcal{P}_h^{\text{sp}}$ and $\mathcal{P}_h^{\text{time}}$ as \mathbf{P}^{sp} and \mathbf{P}^{time} , respectively. These interpolations allow us to define

$$\tilde{L}_h : \mathcal{V}_h \rightarrow \mathcal{V}_h^{d+2}, \quad \tilde{L}_h[u_h] := (\epsilon_\theta u_h, \mathcal{P}_h^{\text{sp}} \nabla_{\Gamma_H}^h u_h, \mathcal{P}_h^{\text{temp}} K_h[u_h]). \quad (14)$$

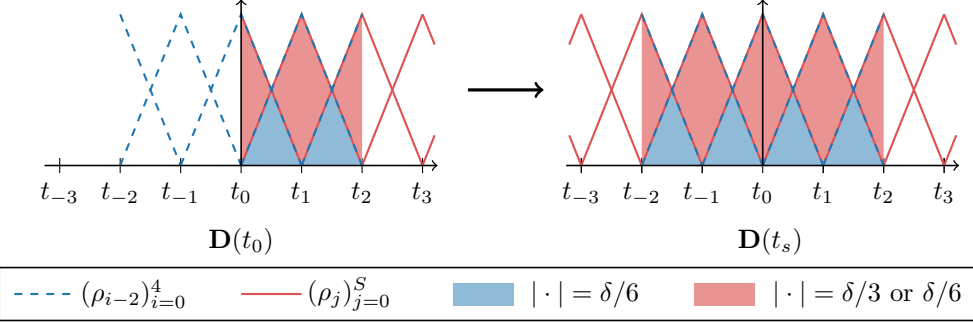


Figure 1: Illustration of the discretized cross-correlation computation of the matrix $\mathbf{D}(t)$ evaluated at the nodes t_s of the uniform mesh with kernel defined in $\tilde{\mathbb{T}} = [t_{-2}, t_2]$. The matrix entries are computed by the overlapping areas of the hat functions.

Since $\mathcal{P}_h^{\text{temp}} K_h[u_h]$ is piecewise affine in time, it suffices to evaluate it at the temporal nodes of \mathcal{S}_h

$$\mathcal{P}_h^{\text{temp}} K_h[u_h](\mathbf{x}, t) = \sum_{i=1}^{N_{\mathcal{V}}} \sum_{s,l=0}^{N_{\mathbb{T}}} \sum_{j=1}^{2N_w} \mathbf{u}_{i,l} \mathbf{k}_j \mathbf{D}_{lj}(t_s) \varphi_i(\mathbf{x}) \rho_s(t).$$

Exploiting uniform timesteps and the relation $t_{s_1} = t_{s_2} + t_{s_3}$ for integers $s_1 = s_2 + s_3$, we obtain the entries of the discretized temporal matrix

$$\begin{aligned} \mathbf{D}(t_s)_{ij} &= \int_{\tilde{\mathbb{T}}} \rho_{i-N_w}(\tau) \rho_j(t_s + \tau) d\tau = \int_{\tilde{\mathbb{T}}} \rho_{i-N_w}(\tau) \rho_{j-s}(\tau) d\tau \\ &= \frac{\delta}{6} \begin{cases} 2, & \text{if } j = (i - N_w) - s, \quad i \in \{0, 2N_w\} \text{ or } j \in \{0, N_{\mathbb{T}}\}, \\ 4, & \text{if } j = (i - N_w) - s, \quad 1 \leq i \leq 2N_w - 1, 1 \leq j \leq N_{\mathbb{T}} - 1, \\ 1, & \text{if } j - ((i - N_w) - s) = 1, \quad i \in \{0, 2N_w\} \text{ or } j \in \{0, N_{\mathbb{T}}\}, \\ 1, & \text{if } |j - ((i - N_w) - s)| = 1, \quad 1 \leq i \leq 2N_w - 1, 1 \leq j \leq N_{\mathbb{T}} - 1, \\ 0, & \text{otherwise.} \end{cases} \end{aligned}$$

The computation of the discrete cross-correlation matrix is illustrated in fig. 1.

3.5 Energy Functionals

Let $\mathcal{J}_h(u_h, z_h)$ denote the finite element discretization of the continuous energy $\mathcal{J}(u, z)$ in (3) such that we aim to optimize

$$\arg \min_{u_h \in \mathcal{V}_h} \{ \mathcal{J}_h(u_h, z_h) := G_h(u_h, z_h) + R_{\theta, h}(u) \}, \quad (15)$$

constructed from the discrete components G_h with

$$G_h(u_h, z_h) = \frac{1}{2N_{\Sigma}} \sum_{i=1}^{N_{\Sigma}} \int_{\mathbb{T}} \left(\int_{\mathcal{T}_{\Sigma_i}} A_h[u_h](\mathbf{x}, t) dS_h^{\Gamma}(\mathbf{x}) - z_{h,i}(t) \right)^2 dt$$

and the regularizer function $R_{\theta, h}$ with potential functions $\tilde{\phi}_i$ of (11)

$$R_{\theta, h}(u_h) = \lambda_{\theta} \sum_{i=1}^{N_C} \int_{\mathcal{T}_h \times \mathbb{T}} \tilde{\phi}_i(L_{h,i}[u_h](\mathbf{x}, t), \tilde{L}_{h,i}[u_h](\mathbf{x}, t)) d\Pi_h(\mathbf{x}, t).$$

We extend the discrete functional in (15) by setting it to $+\infty$ outside \mathcal{V}_h

$$\tilde{\mathcal{J}}_h(u_h, z_h) = \begin{cases} \mathcal{J}_h(u_h, z_h), & \text{if } u_h \in \mathcal{V}_h, \\ +\infty, & \text{else.} \end{cases}$$

For a fixed mesh size $h > 0$, the discrete energies can be expressed as functions of the finite element degrees of freedom by evaluating with quadrature rules to compute the energy explicitly. For the inverse problem, we define the linear operator notation $\tilde{A}[u]_i(t) := \int_{\Sigma_i} A[u](\mathbf{x}, t) dS^\Gamma(\mathbf{x})$ together with its matrix representation $\tilde{\mathbf{A}}$, which is computed using the trapezoidal rule to ensure exact integration for piecewise affine functions. The discrete data fidelity term reads

$$\mathbf{G}_h(\mathbf{u}, \mathbf{z}) = \frac{1}{2}(\tilde{\mathbf{A}}\mathbf{u} - \mathbf{z})^\top \mathbf{D}^\Sigma (\tilde{\mathbf{A}}\mathbf{u} - \mathbf{z}), \quad \text{with } \mathbf{D}^\Sigma = \tilde{\mathbf{D}} \otimes I_{N_\Sigma}.$$

The discrete spatiotemporal regularizer is computed with the lumped quadrature rule

$$\mathbf{R}_{\theta, h}(\mathbf{u}) = \lambda_\theta \sum_{i=1}^{N_C} \sum_{m=0}^{N_T} \sum_{j=1}^{N_V} \mathbf{D}_{mm}^{\text{lump}} \mathbf{M}_{ii}^{\text{lump}} \phi_i \begin{pmatrix} \epsilon_\theta \mathbf{u}_{j,m} \\ (\mathcal{P}_h^{\text{sp}} \nabla_x^h \mathbf{u})_{j,m} \\ (\mathbf{k}_i^\top \mathbf{D}(t_m) (\mathbf{u}_{j,s})_{s=0}^{N_T}) \end{pmatrix},$$

where \mathbf{D}^{lump} and \mathbf{M}^{lump} denote the lumped mass matrices. Remark that we computed the regularizer with ϕ_i instead of $\tilde{\phi}_i$ to omit unnecessary computation in practical applications. This formulation provides a fully discrete representation of the energy functional in terms of the finite element degrees of freedom, facilitating efficient numerical implementation.

Remark 1. *The functional \mathbf{G}_h is an exact representation of G_h since the piecewise affine functions are evaluated with an exact quadrature rule. The joint regularizer $\mathbf{R}_{\theta, h}$ converges with order $O(h^2)$.*

3.6 Geometric Approximation and Lifting

Following [9], we define lifting of functions between discretized and true domains. We begin by introducing the bijective lifting from the discretized spatial domains to the continuous domain. The normal projection $\mathbf{x} \mapsto p(\mathbf{x})$ from a narrow band around $\partial\Omega_0$ is then defined as the unique solution of $\mathbf{x} = p(\mathbf{x}) + d(\mathbf{x})\mathbf{n}(p(\mathbf{x}))$ with the distance function

$$d(\mathbf{x}) = \begin{cases} -\inf_{\mathbf{y} \in \partial\Omega_0} \{|\mathbf{x} - \mathbf{y}|\}, & \mathbf{x} \in \Omega_0, \\ \inf_{\mathbf{y} \in \partial\Omega_0} \{|\mathbf{x} - \mathbf{y}|\}, & \mathbf{x} \notin \overline{\Omega}_0, \end{cases}$$

and the normal to the boundary $\mathbf{n}(\mathbf{x}) = \nabla_{\mathbf{x}} d(\mathbf{x})$ for almost every $\mathbf{x} \in \partial\Omega_0$. We assume that h is chosen small enough such that all vertices of \mathcal{T}_h lie within a narrow band where the distance function and closest point projection are well defined. Furthermore, the surface gradient of a function $v : \Gamma_H \rightarrow \mathbb{R}$ is defined as $\nabla_{\Gamma_H} v = (\mathbf{I}_d - \mathbf{n} \otimes \mathbf{n}) \nabla_{\mathbf{x}} v$ with $\nabla_{\mathbf{x}} v$ the gradient in the ambient coordinates of an arbitrary extension of v to the narrow band. The definition of the homeomorphism $H_h : \mathcal{U}_h \rightarrow \Omega_0$ follows [9] by mapping each element of the computational domain back to a reference element and then to the true curved domain. Denote the mapping from the reference element \hat{J} to an element $J \in \mathcal{U}_h$ by M_J and the mapping from the reference element to the curved element J^e representing the true domain with curved boundary by M_J^e . Then

$$H_h(\mathbf{x}) = M_J^e((M_J)^{-1}(\mathbf{x})).$$

Restricted to the interior elements, the homeomorphism H_h coincides with the identity. Figure 2 illustrates the lifting of a boundary simplex in \mathbb{R}^2 . A similar illustration for \mathbb{R}^3 can be seen in [9].

To describe the local behavior of the discrete boundary mapping near $\partial\Omega_0$, we use the following estimates. For boundary elements $J \in \partial\mathcal{U}_h$ that have more than one vertex on $\partial\Omega_0$, the homeomorphism satisfies

$$\|\nabla_{\mathbf{x}} H_h^\top|_J - \text{Id}\|_{L^\infty(J)} \leq ch \quad \text{and} \quad \|\det \nabla_{\mathbf{x}} H_h^\top|_J - 1\|_{L^\infty(J)} \leq ch,$$

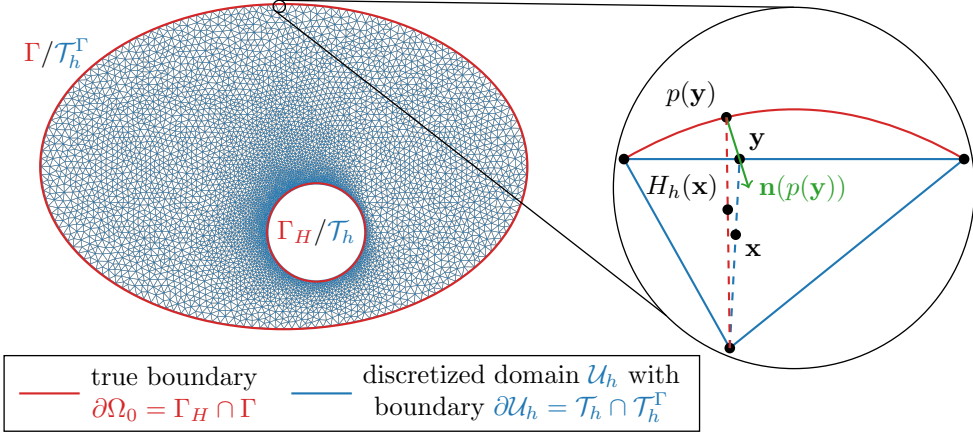


Figure 2: Lifting of the \mathbf{x} point in a simplex at a boundary element $J \subset \mathcal{U}_h$ to the true domain by $H_h(\mathbf{x}) \in J^e \subset \Omega_0$ in \mathbb{R}^2 . We compute the linear projection \mathbf{y} of \mathbf{x} onto the boundary \mathcal{T}_h^Γ , take the closest-point projection $p(\mathbf{y})$ on Γ , and map \mathbf{x} towards $p(\mathbf{y})$ to compute $H_h(\mathbf{x})$.

where $c > 0$ is a constant independent of h . Furthermore, for any discretization $\partial\mathcal{U}_h$ of the boundary of $\partial\Omega_0$, we define the quotient of measures ν_h and ν_h^Γ such that $dS = \nu_h dS_h$ and $dS^\Gamma(\mathbf{x}) = \nu_h dS_h^\Gamma(\mathbf{x})$ for surface measures S_h and S_h^Γ of \mathcal{T}_h and \mathcal{T}_h^Γ , respectively. The measures account for the geometric difference between the manifold and its discretizations, satisfying

$$\sup_{\mathcal{T}_h} \{|1 - \nu_h|\} \leq ch \quad \text{and} \quad \sup_{\mathcal{T}_h^\Gamma} \{|1 - \nu_h^\Gamma|\} \leq ch. \quad (16)$$

As a result, we define a projection lifting a discretized signal to the continuous domain.

Definition 1 (Lift and inverse lift). *For a function $v_h : \mathcal{U}_h \rightarrow \mathbb{R}$ we define its lift by $v_h^l := v_h \circ H_h^{-1}$ on Ω_0 , and for $v : \Omega_0 \rightarrow \mathbb{R}$ its inverse lift by $v^{-l} := v \circ H_h$ on \mathcal{U}_h . Analogously, for $u_h : \partial\mathcal{U}_h \rightarrow \mathbb{R}$ the lift $u_h^l : \partial\Omega_0 \rightarrow \mathbb{R}$ is defined by $u_h^l(p(\mathbf{x})) := u_h(\mathbf{x})$, and for $u : \partial\Omega_0 \rightarrow \mathbb{R}$ the inverse lift by $u^{-l}(\mathbf{x}) := u(p(\mathbf{x}))$.*

As a consequence of these definitions, functions and their lifts are comparable in the relevant Sobolev norms, see [9, Proposition 4.9, 4.13].

Proposition 1 (Norm equivalence under lifting). *Let $v_h : \mathcal{U}_h \rightarrow \mathbb{R}$ and $u_h : \partial\mathcal{U}_h \rightarrow \mathbb{R}$ with lifts $v_h^l : \Omega_0 \rightarrow \mathbb{R}$ and $u_h^l : \partial\Omega_0 \rightarrow \mathbb{R}$. Then the L^2 - and H^1 -norms of v_h and u_h are equivalent to the corresponding norms of their lifts. The equivalence constants are independent of the discretization parameter h .*

4 Convergence

In this section, we prove the Mosco convergence of the finite element discretized energy to the corresponding continuous energy under the convex regularization framework, i.e., assuming that the potential functions ϕ_i in (7) are convex for $i = 1, \dots, N_C$. Moreover, we establish the convergence of minimizers. The proof exploits some concepts of [21]. We start by defining the topology for convergence.

Definition 2. (\mathcal{Z} -topology) *Let Γ_H be a surface with discretizations defined by $(\mathcal{T}_h)_h$, and let $(\mathcal{U}_h)_h$ be a family of shape-regular bulk discretizations of Ω_0 . We say that $(u_h)_h$ on $\mathcal{T}_h \times \mathcal{S}_h$ converges weakly to $u \in \mathcal{V}$ w.r.t. the \mathcal{Z} -topology denoted by $u_h \xrightarrow{\mathcal{Z}} u$ if*

and only if the lifted functions satisfy $u_h^l \xrightarrow{\mathcal{V}} u$. We say that $(u_h)_h$ converges strongly to u w.r.t. the \mathcal{Z} -topology $u_h \xrightarrow{\mathcal{Z}} u$ if and only if $u_h^l \xrightarrow{\mathcal{V}} u$.

We recall the definition of Mosco convergence [20].

Definition 3. (Mosco-convergence) Functionals $\mathcal{J}_h : \mathcal{V}_h \rightarrow \overline{\mathbb{R}}$ for $h > 0$ are said to converge to $\mathcal{J} : \mathcal{V} \rightarrow \overline{\mathbb{R}}$ in the sense of Mosco w.r.t. the \mathcal{Z} -topology if

1. for every sequence $(u_h)_h \subset \mathcal{V}_h$ with $u_h \xrightarrow{\mathcal{Z}} u$ the functional inequality $\mathcal{J}_h(u) \leq \liminf_{h \rightarrow 0} \mathcal{J}_h(u_h)$ holds true ('liminf-inequality').
2. for every $u \in \mathcal{V}$ there exists a recovery sequence $(u_h)_h \subset \mathcal{V}_h$ such that $u_h \xrightarrow{\mathcal{V}} u$ and $\mathcal{J}(u) \geq \limsup_{h \rightarrow 0} \mathcal{J}_h(u_h)$ ('limsup-inequality').

If in 1. the strong convergence $u_h \xrightarrow{\mathcal{V}} u$ is required, then \mathcal{J}_h is said to Γ -converge to \mathcal{J} with respect to the \mathcal{Z} -topology.

First, we prove the convergence of the discrete operator \tilde{L}_h defined in (14) to the continuous operator $L = (\epsilon_\theta u, \nabla_{\Gamma_H} u, K[u])$.

Lemma 1. Let $(u_h)_h \subset \mathcal{V}_h$ be a sequence whose lifts u_h^l converge weakly in \mathcal{V} to some $u \in \mathcal{V}$. Assume that the kernels k_h converge strongly to k in $L^1(T)$. Then the lifted operator $\tilde{L}_h^l[u_h^l] := (\epsilon_\theta u_h^l, (\mathcal{P}_h^{\text{sp}} \nabla_{\Gamma_H}^h u_h)^l, K_h[u_h^l])$ converges weakly in $\mathcal{Y}^{d+2} = \mathcal{Y} \times \mathcal{Y}^d \times \mathcal{Y}$ to $L[u]$. Moreover, if u_h^l converges strongly to u in \mathcal{V} , then $\tilde{L}_h^l[u_h^l]$ converges strongly to $L[u]$ in \mathcal{Y}^{d+2} .

Proof. Assume that $u_h^l \rightharpoonup u$ weakly in \mathcal{V} . We prove the weak convergence of $\tilde{L}_h^l[u_h^l]$ componentwise in \mathcal{Y}^{d+2} . For the first component, we have $\epsilon_\theta u_h^l \rightharpoonup \epsilon_\theta u$ in \mathcal{Y} , which follows directly from the weak convergence of u_h^l in \mathcal{V} and the continuous embedding $\mathcal{V} \hookrightarrow \mathcal{Y}$. For the spatial gradient component, let $\varphi \in \mathcal{Y}^d$ be an arbitrary test function and compute

$$\int_{\Gamma_H \times \mathbb{T}} (\mathcal{P}_h^{\text{sp}} \nabla_{\Gamma_H}^h u_h)^l \cdot \varphi d\Pi(\mathbf{x}, t) = \int_{\mathcal{T}_h \times \mathbb{T}} \nabla_{\Gamma_H}^h u_h \cdot \mathcal{P}_h^{\text{sp}} \varphi^{-l} \nu_h d\Pi_h(\mathbf{x}, t),$$

where $d\Pi_h(\mathbf{x}, t) := dS_h(\mathbf{x}) \otimes d\lambda(t)$ and the last equality follows from self-adjointness of the L^2 -projection $\mathcal{P}_h^{\text{sp}}$ on \mathcal{Y}_h^d . We then decompose the integrand as

$$\begin{aligned} \int_{\mathcal{T}_h \times \mathbb{T}} \nabla_{\Gamma_H}^h u_h \cdot \mathcal{P}_h^{\text{sp}} \varphi^{-l} \nu_h d\Pi_h(\mathbf{x}, t) &= \int_{\mathcal{T}_h \times \mathbb{T}} \nabla_{\Gamma_H}^h u_h \cdot \varphi^{-l} \nu_h d\Pi_h(\mathbf{x}, t) \\ &\quad + \int_{\mathcal{T}_h \times \mathbb{T}} \nabla_{\Gamma_H}^h u_h \cdot (\mathcal{P}_h^{\text{sp}} \varphi^{-l} - \varphi^{-l}) \nu_h d\Pi_h(\mathbf{x}, t). \end{aligned}$$

For the first term, the weak convergence of the lifted discrete gradients, $(\nabla_{\Gamma_H}^h u_h)^l \rightharpoonup \nabla_{\Gamma_H} u$ in \mathcal{Y}^d , together with the change of variables from \mathcal{T}_h to Γ_H , gives

$$\int_{\mathcal{T}_h \times \mathbb{T}} \nabla_{\Gamma_H}^h u_h \cdot \varphi^{-l} \nu_h d\Pi_h(\mathbf{x}, t) \rightarrow \int_{\Gamma_H \times \mathbb{T}} \nabla_{\Gamma_H} u \cdot \varphi d\Pi(\mathbf{x}, t)$$

as $h \rightarrow 0$. For the second term, we apply the Cauchy–Schwarz inequality together with the uniform boundedness of $\nabla_{\Gamma_H}^h u_h$ in $L^2(\mathcal{T}_h \times \mathbb{T})$ such that

$$\begin{aligned} &\left| \int_{\mathcal{T}_h \times \mathbb{T}} \nabla_{\Gamma_H}^h u_h \cdot (\mathcal{P}_h^{\text{sp}} \varphi^{-l} - \varphi^{-l}) \nu_h d\Pi_h(\mathbf{x}, t) \right| \\ &\leq C \min_{v_h^l \in (\mathcal{Y}_h^l)^d} \left(\int_{\Gamma_H \times \mathbb{T}} |v_h^l - \varphi|^2 d\Pi(\mathbf{x}, t) \right)^{1/2}. \end{aligned}$$

By the denseness in $\|\cdot\|_{\mathcal{Y}^d}$, this last term tends to 0 as $h \rightarrow 0$. Hence we conclude that $(\mathcal{P}_h^{\text{sp}} \nabla_{\Gamma_H}^h u_h)^l \rightharpoonup \nabla_{\Gamma_H} u$ in \mathcal{Y}^d . For the last component, $K_h[u_h^l]$, we first show the weak convergence of the temporal cross-correlation $k_h *_{\mathbb{T}} u_h^l \rightharpoonup k *_{\mathbb{T}} u$ in \mathcal{Y} . Define the flipped kernel functions $\tilde{k}_h(t) := k_h(-t)$ and $\tilde{k}(t) := k(-t)$ with $\tilde{k}_h \rightarrow \tilde{k}$ strongly in $L^1(\mathbb{T})$. For any test function $\varphi \in \mathcal{Y}$, we decompose

$$(k_h *_{\mathbb{T}} u_h^l, \varphi)_{\mathcal{Y}} = (u_h^l, \tilde{k} *_{\mathbb{T}} \varphi)_{\mathcal{Y}} + (u_h^l, (\tilde{k}_h - \tilde{k}) *_{\mathbb{T}} \varphi)_{\mathcal{Y}}.$$

The second term vanishes as $h \rightarrow 0$ by Cauchy–Schwarz and Young’s inequality together with $\|\tilde{k}_h - \tilde{k}\|_{L^1(\mathbb{T})} \rightarrow 0$. The first term converges to $(k *_{\mathbb{T}} u, \varphi)_{\mathcal{Y}}$ by weak convergence of u_h^l in \mathcal{Y} . Including the temporal interpolation operator, we write

$$(\mathcal{P}_h^{\text{temp}}(k_h *_{\mathbb{T}} u_h^l), \varphi)_{\mathcal{Y}} = (k_h *_{\mathbb{T}} u_h^l, \varphi)_{\mathcal{Y}} + (\mathcal{P}_h^{\text{temp}}(k_h *_{\mathbb{T}} u_h^l) - k_h *_{\mathbb{T}} u_h^l, \varphi)_{\mathcal{Y}},$$

where the additional term vanishes as $h \rightarrow 0$ by (12). The first term converges weakly as shown above. Hence, we conclude $(\mathcal{P}_h^{\text{temp}}(k_h *_{\mathbb{T}} u_h^l)) \rightharpoonup k *_{\mathbb{T}} u$ in \mathcal{Y} , completing the proof for the temporal component and weak convergence.

Next, assume that $u_h^l \rightarrow u$ strongly in \mathcal{Y} . We again prove the strong convergence of $\tilde{L}_h^l[u_h^l]$ componentwise in \mathcal{Y}^{d+2} . For the first component, strong convergence follows directly from the assumption $\epsilon_{\theta} u_h^l \rightarrow \epsilon_{\theta} u$ in \mathcal{Y} . For the spatial gradient, we decompose the convergence error using an intermediate approximation $v_h \in \mathcal{V}_h$ which is a piecewise affine function whose lift satisfies $v_h^l \rightarrow \nabla_{\Gamma_H} u$ strongly in \mathcal{Y}^d . The existence of such a sequence is guaranteed by the approximation property of $(\mathcal{Y}_h^l)^d$. We then write

$$\begin{aligned} \|(\mathcal{P}_h^{\text{sp}} \nabla_{\Gamma_H}^h u_h)^l - \nabla_{\Gamma_H} u\|_{\mathcal{Y}^d} &\leq \|(\mathcal{P}_h^{\text{sp}} \nabla_{\Gamma_H}^h u_h)^l - (\mathcal{P}_h^{\text{sp}} v_h)^l\|_{\mathcal{Y}^d} \\ &\quad + \|(\mathcal{P}_h^{\text{sp}} v_h)^l - v_h^l\|_{\mathcal{Y}^d} + \|v_h^l - \nabla_{\Gamma_H} u\|_{\mathcal{Y}^d}. \end{aligned}$$

For the first term, lifting back to \mathcal{T}_h and using the stability of $\mathcal{P}_h^{\text{sp}}$ gives

$$\begin{aligned} \|(\mathcal{P}_h^{\text{sp}} \nabla_{\Gamma_H}^h u_h)^l - (\mathcal{P}_h^{\text{sp}} v_h)^l\|_{\mathcal{Y}^d}^2 &= \int_{\mathcal{T}_h \times \mathbb{T}} |\mathcal{P}_h^{\text{sp}}(\nabla_{\Gamma_H}^h u_h - v_h)|^2 \nu_h \, d\Pi_h(\mathbf{x}, t) \\ &\leq \int_{\mathcal{T}_h \times \mathbb{T}} |\nabla_{\Gamma_H}^h u_h - v_h|^2 \nu_h \, d\Pi_h(\mathbf{x}, t) \leq \|(\nabla_{\Gamma_H}^h u_h)^l - \nabla_{\Gamma_H} u\|_{\mathcal{Y}^d}^2 + \|\nabla_{\Gamma_H} u - v_h^l\|_{\mathcal{Y}^d}^2, \end{aligned}$$

which converges to 0 as $h \rightarrow 0$ by the strong convergence assumption and the choice of v_h . The second term vanishes exactly, since $\mathcal{P}_h^{\text{sp}} v_h = v_h$. The third term converges to 0 by construction of v_h . Hence we conclude $(\mathcal{P}_h^{\text{sp}} \nabla_{\Gamma_H}^h u_h)^l \rightarrow \nabla_{\Gamma_H} u$ strongly in \mathcal{Y}^d . Finally, we prove the strong convergence of the temporal cross-correlation component. We decompose the error as

$$\begin{aligned} \|K_h[u_h^l] - K[u]\|_{\mathcal{Y}} &\leq \|K_h[u_h^l] - (k_h *_{\mathbb{T}} u_h^l)\|_{\mathcal{Y}} \\ &\quad + \|(k_h *_{\mathbb{T}} u_h^l) - (k *_{\mathbb{T}} u_h^l)\|_{\mathcal{Y}} + \|K[u_h^l] - K[u]\|_{\mathcal{Y}}. \end{aligned}$$

For the first term, the temporal interpolation estimate (12) gives

$$\|K_h[u_h^l] - (k_h *_{\mathbb{T}} u_h^l)\|_{\mathcal{Y}} \leq Ch^2 \|\partial_{tt}(k_h *_{\mathbb{T}} u_h^l)\|_{\mathcal{Y}} \rightarrow 0.$$

The second term is bounded using Young’s inequality

$$\|(k_h *_{\mathbb{T}} u_h^l) - (k *_{\mathbb{T}} u_h^l)\|_{\mathcal{Y}} \leq \|k_h - k\|_{L^1(\mathbb{T})} \|u_h^l\|_{\mathcal{Y}} \rightarrow 0$$

since $k_h \rightarrow k$ in $L^1(\mathbb{T})$. For the last term, Young’s inequality yields

$$\|K[u_h^l] - K[u]\|_{\mathcal{Y}} \leq \|k\|_{L^1(\mathbb{T})} \|u_h^l - u\|_{\mathcal{Y}} \rightarrow 0$$

due to the strong convergence $u_h^l \rightarrow u$ in \mathcal{Y} . Combining these three estimates, we conclude $K_h[u_h^l] \rightarrow K[u]$ strongly in \mathcal{Y} , which completes the proof of strong convergence for the temporal cross-correlation and the strong convergence. \square

Remark 2. The weak and strong convergence results of lemma 1 also hold for the operator L_h in (10) in place of \tilde{L}_h . Both discretizations converge to the same limit operator $L[u]$ in \mathcal{Y}^{d+2} .

Next, we consider the convergence of the solution of the forward problem.

Lemma 2. Let $v \in L^2(\mathbb{T}; H^1(\Omega_0))$ be the weak solution of (1) w.r.t. $u \in \mathcal{V}$. For each $h > 0$, denote by $v_h \in P_1(\mathcal{U}_h) \otimes P_1(\mathcal{S}_h)$ the weak solution of the discretized forward problem (2) with boundary condition $u_h \in \mathcal{V}_h$. Let u_h^l and v_h^l denote the lifted functions. Then the following statements hold:

1. If $u_h^l \rightharpoonup u$ weakly in \mathcal{V} , then $v_h^l \rightharpoonup v$ weakly in $L^2(\mathbb{T}; H^1(\Omega_0))$.
2. If $u_h^l \rightarrow u$ strongly in \mathcal{V} , then $v_h^l \rightarrow v$ strongly in $L^2(\mathbb{T}; H^1(\Omega_0))$.

Proof. By lifting the function, we can rewrite (8) as finding v_h^l with epicardium boundary function u_h^l such that

$$a_h^l(v_h^l(\cdot, t), \varphi_h^l) := \int_{\Omega_0} \sigma_h(\mathbf{x}) \nabla_{\mathbf{x}} H_h^{\top} \nabla_x \mathbf{x} v_h^l(\mathbf{x}, t) \cdot (\nabla_{\mathbf{x}} H_h^{\top} \nabla_{\mathbf{x}} \varphi_h^l(\mathbf{x})) \frac{1}{|\det \nabla_{\mathbf{x}} H_h^{\top}|} d\mathbf{x} = 0,$$

for all $\varphi_h^l \in (P_1(\mathcal{U}_h))^l$ with $\varphi_h^l|_{\Gamma_H} = 0$. Coercivity and continuity follow analogously. Then, we rewrite the weak problem as in (9) using $v_h^l = w_h^l + g_h^l$, which yields

$$a_h^l(w_h^l(\cdot, t), \varphi_h^l) = -a_h^l(g_h^l(\cdot, t), \varphi_h^l) \quad \forall \varphi_h^l \in P_1(\mathcal{U}_h), \varphi_h^l|_{\Gamma_H} = 0.$$

Testing with $\varphi_h^l = w_h^l(\cdot, t)$ for almost all $t \in \mathbb{T}$ yields

$$\|w_h^l(\cdot, t)\|_{H^1(\Omega_0)} \leq C \|g_h^l(\cdot, t)\|_{H^1(\Omega_0)}.$$

Hence, there exists an upper bound on the solution to the problem

$$\|v_h^l(\cdot, t)\|_{H^1(\Omega_0)} \leq \|g_h^l(\cdot, t)\|_{H^1(\Omega_0)} + \|w_h^l(\cdot, t)\|_{H^1(\Omega_0)} \leq C \|u_h^l(\cdot, t)\|_{H^{1/2}(\Gamma_H)}.$$

By integrating over \mathbb{T} , we prove an upper bound in $L^2(\mathbb{T}; H^1(\Omega_0))$ and by weak compactness up to a subsequence, we have $v_h^l \rightharpoonup \tilde{v}$ weakly in $L^2(\mathbb{T}; H^1(\Omega_0))$. Choose any $\varphi \in H^1(\Omega_0)$ with $\varphi|_{\Gamma_H} = 0$ and a sequence $\varphi_h^l \rightarrow \varphi$ strongly in $H^1(\Omega_0)$ with $\varphi_h \in P_1(\mathcal{U}_h)$, then by consistency of the lifting, we have

$$\int_{\mathbb{T}} a_h^l(v_h^l(\cdot, t), \varphi_h^l) dt \rightarrow \int_{\mathbb{T}} a(\tilde{v}(\cdot, t), \varphi) dt \quad \text{with} \quad a(\tilde{v}(\cdot, t), \varphi) = 0 \quad \text{for a.e. } t \in \mathbb{T}.$$

Moreover, for almost every $t \in \mathbb{T}$, $\tilde{v}(\cdot, t)|_{\Gamma_H} = u(\cdot, t)$ and by uniqueness of the continuous problem $\tilde{v}(\cdot, t) = v(\cdot, t)$ which proves the weak convergence in $L^2(\mathbb{T}; H^1(\Omega_0))$.

Next, we assume that $u_h^l \rightarrow u$ strongly in \mathcal{V} . For almost all $t \in T$, there exists an upper bound on the true solution to the problem

$$\|v(\cdot, t) - v_h^l(\cdot, t)\|_{H^1(\Omega_0)} \leq \|g(\cdot, t) - g_h^l(\cdot, t)\|_{H^1(\Omega_0)} + \|w(\cdot, t) - w_h^l(\cdot, t)\|_{H^1(\Omega_0)}.$$

The first part of the sum can be estimated from above by the trace extension operator on the epicardium, such that

$$\|g(\cdot, t) - g_h^l(\cdot, t)\|_{H^1(\Omega_0)} \leq C_E \|u(\cdot, t) - u_h^l(\cdot, t)\|_{H^{1/2}(\Omega_0)},$$

which vanishes by assumption. For the upper bound of the second error, we refer the reader to [9, Theorem 6.1]. Integrating over time yields strong convergence in \mathcal{V} . \square

Next, we prove the convergence of the energy functionals.

Lemma 3. Let R_θ be convex, $z_h \rightarrow z$ in $(L^2(T))^{N_\Sigma}$, and $k_{h,i} \rightarrow k_i$ in $L^1(\mathbb{T})$ for $i = 1, \dots, N_C$. Then for any sequence $(u_h)_h \subset \mathcal{V}_h$ with $u_h \xrightarrow{\mathcal{Z}} u \in \mathcal{V}$, we have $G(u, z) \leq \liminf_{h \rightarrow 0} G_h(u_h, z_h)$ and $R_\theta(u) \leq \liminf_{h \rightarrow 0} R_{\theta,h}(u_h)$. If $u_h \xrightarrow{\mathcal{Z}} u$, then $G(u, z) = \lim_{h \rightarrow 0} G_h(u_h, z_h)$ and $R_\theta(u) = \lim_{h \rightarrow 0} R_{\theta,h}(u_h)$.

Proof. Assume that $u_h \xrightarrow{\mathcal{Z}} u$ and therefore $u_h^l \xrightarrow{\mathcal{V}} u$. Denote by v_h^l the lifted solution with respect to the boundary condition u_h^l of the weak formulation (8). By lemma 2, we know that $v_h^l \xrightarrow{\mathcal{V}} v$. Define A_h^l as the lifted operator depending on the lifted solution v_h^l of the discretized problem (2) for boundary condition u_h^l . By concatenation with the linear bounded trace operator, weak convergence is preserved $A_h^l[u_h^l] \xrightarrow{\mathcal{V}} A[u]$. The results follow from the lower semicontinuity of D and the strong convergence of z_h .

Since the ϕ_i are convex and continuous in all arguments, R_θ is weak lower semicontinuous and we have together with Lemma 1

$$\begin{aligned} R_\theta(u) &\leq \liminf_{h \rightarrow 0} \lambda_\theta \sum_{i=1}^{N_C} \int_{\Gamma_H \times \mathbb{T}} \phi_i(L_{h,i}^l[u_h^l](\mathbf{x}, t), \tilde{L}_{h,i}^l[u_h^l](\mathbf{x}, t)) d\Pi(\mathbf{x}, t) \\ &= \liminf_{h \rightarrow 0} \lambda_\theta \sum_{i=1}^{N_C} \int_{\mathcal{T}_h \times \mathbb{T}} \phi_i(L_{h,i}[u_h](\mathbf{x}, t), \tilde{L}_{h,i}[u_h](\mathbf{x}, t)) \nu_h d\Pi_h(\mathbf{x}, t). \end{aligned}$$

By (16), we can drop ν_h in the limit $h \rightarrow 0$ and conclude $R_\theta(u) \leq \liminf_{h \rightarrow 0} R_{\theta,h}(u_h)$. Assume $u_h \xrightarrow{\mathcal{Z}} u$, then the lifted sequence converges $u_h^l \xrightarrow{\mathcal{V}} u$, lemma 2 together with the trace theorem yield for almost every $t \in \mathbb{T}$ and $i = 1, \dots, N_\Sigma$

$$\|A[u](\cdot, t) - A_h^l[u_h^l](\cdot, t)\|_{H^{1/2}(\Sigma_i)} \leq C_T \|v(\cdot, t) - v_h^l(\cdot, t)\|_{H^1(\Omega_0)} \rightarrow 0.$$

Moreover, we can write by Cauchy-Schwarz and the embedding of L^1 in L^2 for bounded domains

$$\left| \int_{\Sigma_i} A[u](\mathbf{x}, t) - A_h^l[u_h^l](\mathbf{x}, t) dS^\Gamma(\mathbf{x}) \right|^2 \leq \frac{1}{|\Sigma_i|} \|A[u](\cdot, t) - A_h^l[u_h^l](\cdot, t)\|_{L^2(\Sigma_i)}^2 \rightarrow 0.$$

Therefore, together with the strong convergence of z_h

$$\int_{\mathbb{T}} \left(\int_{\Sigma_i} A[u] dS^\Gamma(\mathbf{x}) - z_i \right)^2 dt = \int_{\mathbb{T}} \left(\int_{\Sigma_i} A_h^l[u_h^l] dS^\Gamma(\mathbf{x}) - z_{h,i} \right)^2 dt + o(1).$$

By applying the inverse lifting to the boundary manifold subject to $A_h^l[u_h^l](p(\mathbf{x}), t) = A_h[u_h](\mathbf{x}, t)$, we can rewrite it such that

$$\int_{\mathbb{T}} \left(\int_{\Sigma_i} A_h^l[u_h^l] dS^\Gamma(\mathbf{x}) - z_{h,i} \right)^2 dt = \int_{\mathbb{T}} \left(\int_{\mathcal{T}^{\Sigma_i}} A_h[u_h] dS_h^\Gamma(\mathbf{x}) - z_{h,i} \right)^2 dt + o(1).$$

Summing over all electrodes $i = 1, \dots, N_\Sigma$ and scaling by $(2N_\Sigma)^{-1}$ yields the claim.

We show the convergence of the regularizer by the dominated convergence theorem. By Lemma 1, $u_h^l \xrightarrow{\mathcal{V}} u$ implies that $\tilde{L}_{h,i}^l[u_h^l] \xrightarrow{\mathcal{V}^{d+2}} L[u]$. Thus, there exists a subsequence such that $\tilde{L}_{h,i}^l[u_h^l](\mathbf{x}, t) \rightarrow L[u](\mathbf{x}, t)$ for almost every $(\mathbf{x}, t) \in \Gamma_H \times \mathbb{T}$. Since the ϕ_i are continuous in all arguments, we get

$$\tilde{\phi}_i(L_{h,i}^l[u_h^l](\mathbf{x}, t), \tilde{L}_{h,i}^l[u_h^l](\mathbf{x}, t)) \rightarrow \phi_i(L[u](\mathbf{x}, t)) \quad \text{for almost every } (\mathbf{x}, t) \in \Gamma_H \times \mathbb{T}.$$

For integrability, we need to show a growth estimate on $\tilde{\phi}_i$. We start with bounding $\tilde{\omega}_\mu^{d+2}$ from above $\|\text{Proj}_{B_{\ell^1}}(\mathbf{y}/\mu)\|_2 \leq \|\text{Proj}_{B_{\ell^1}}(\mathbf{y}/\mu)\|_1 \leq 1$ and by the triangle inequality

$$\left\| \mathbf{y} - \mu \text{Proj}_{B_{\ell^1}}(\mathbf{y}/\mu) \right\|_\infty \leq \|\mathbf{y}\|_\infty + \mu \left\| \text{Proj}_{B_{\ell^1}}(\mathbf{y}/\mu) \right\|_\infty \leq \|\mathbf{y}\|_2 + \mu.$$

Both combined ensure the boundedness $\tilde{\omega}_\mu^{d+2}(\mathbf{y}, \tilde{\mathbf{y}}) \leq C_1 + C_2(\|\mathbf{y}\|_2^2 + \|\tilde{\mathbf{y}}\|_2^2)$ and by the boundedness of $\|\mathbf{Q}_i\|$, we have the growth condition

$$\tilde{\phi}_i(\mathbf{y}, \tilde{\mathbf{y}}) = \mu_i \tilde{\omega}_{\mu_i}^{d+2}(\mathbf{y}, \tilde{\mathbf{y}}) + \mu_i \tilde{\omega}_{\eta_i \mu_i}^{d+2}(\mathbf{Q}_i \mathbf{y}, \mathbf{Q}_i \tilde{\mathbf{y}}) \leq \tilde{C}_1 + \tilde{C}_2(\|\mathbf{y}\|_2^2 + \|\tilde{\mathbf{y}}\|_2^2).$$

Therefore, $\tilde{\phi}_i(L_{h,i}^l[u_h^l](\mathbf{x}, t), \tilde{L}_{h,i}^l[u_h^l](\mathbf{x}, t))$ is uniformly integrable in $L^1(\Gamma_H \times T)$ and dominated convergence yields

$$\begin{aligned} R_\theta(u) &= \lim_{h \rightarrow 0} \lambda_\theta \sum_{i=1}^{N_C} \int_{\Gamma_H \times \mathbb{T}} \tilde{\phi}_i(L_{h,i}^l[u_h^l](\mathbf{x}, t), \tilde{L}_{h,i}^l[u_h^l](\mathbf{x}, t)) d\Pi(\mathbf{x}, t) \\ &= \lim_{h \rightarrow 0} \lambda_\theta \sum_{i=1}^{N_C} \int_{\mathcal{T}_h \times \mathbb{T}} \tilde{\phi}_i(L_{h,i}[u_h](\mathbf{x}, t), \tilde{L}_{h,i}[u_h](\mathbf{x}, t)) \nu_h d\Pi_h(\mathbf{x}, t) = R_{\theta,h}(u_h). \end{aligned}$$

□

Next, we prove Mosco-convergence and convergence of minimizers.

Theorem 2. (*Mosco-convergence*) *Let the assumptions of Lemma 3 be satisfied. Then $\tilde{\mathcal{J}}_h$ Mosco-converges to \mathcal{J} with respect to the \mathcal{Z} -topology.*

Proof. ('liminf-inequality') Let $(u_h)_h \subset \mathcal{V}_h$ be a sequence such that $u_h \xrightarrow{\mathcal{Z}} u \in \mathcal{V}$. Thus, we have $u_h^l \xrightarrow{\mathcal{V}} u$ for the projection u_h^l of u_h . By construction of $u_h \in \mathcal{V}_h$, we have $\sup_{h>0} \{\tilde{\mathcal{J}}_h(u_h, z_h)\} < \infty$. Then, by lemma 3, it follows that

$$R_\theta(u) \leq \liminf_{h \rightarrow 0} R_\theta(u_h) \quad \text{and} \quad D(u, z) \leq \liminf_{h \rightarrow 0} D(u_h^l, z).$$

Combining these results, we obtain $\mathcal{J}(u, z) \leq \liminf_{h \rightarrow 0} \tilde{\mathcal{J}}_h(u_h, z_h)$, which establishes the liminf condition.

('limsup-inequality') Since Γ_H is a closed Riemannian manifold, $C^\infty(\Gamma_H)$ is dense in $H^1(\Gamma_H)$ as proven in [16]. Applying mollification in time to $u \in \mathcal{V}$, we obtain $u * p_\eta \in C^\infty(\overline{\mathbb{T}}; H^1(\Gamma_H))$ converging in \mathcal{V} as $\eta \rightarrow 0$. Hence, we can construct a smooth sequence $(u_n)_n \subset C^\infty(\Gamma_H \times \overline{\mathbb{T}})$ such that $u_n \xrightarrow{\mathcal{V}} u$. For each u_n , we construct a sequence $(u_{n,h}^l)_h$ with $u_{n,h}^l \xrightarrow{\mathcal{V}} u_n$. Selecting a diagonal subsequence $h = h(n)$ yields a recovery sequence $u_{h(n)}^l \xrightarrow{\mathcal{V}} u$. Proposition 1 and integration over time implies that if $u_h^l \in \mathcal{V}$ then $u_h \in L^2(T; H^1(\mathcal{T}_h))$ and the interpolation error vanishes as $h \rightarrow 0$. Finally, applying lemma 3 gives

$$\lim_{h \rightarrow 0} \tilde{\mathcal{J}}_h(u_h, z_h) = \lim_{h \rightarrow 0} G_h(u_h, z_h) + R_\theta(u_h) = G(u, z) + R(u, z) = \mathcal{J}(u, z),$$

which establishes the limsup inequality and completes the proof. □

Finally, we establish convergence of the discrete minimizers to the continuous ones.

Theorem 3. (*Convergence of minimizers*) *Let the assumptions of Lemma 3 be satisfied and $(u_h)_h \subset \mathcal{V}_h$ be a sequence of minimizers of the discrete energies $\tilde{\mathcal{J}}_h$. Then, the sequence $(u_h)_h$ converges weakly (up to a subsequence) in the \mathcal{Z} -topology to a minimizer of \mathcal{J} , and $\lim_{h \rightarrow 0} \inf_{u_h \in \mathcal{V}_h} \{\tilde{\mathcal{J}}_h(u_h, z_h)\} = \inf_{u \in \mathcal{V}} \{\mathcal{J}(u, z)\}$.*

Proof. Since the sequence of minimizers is constructed in \mathcal{V}_h , we have for the discrete energy $\sup_{h>0} \{\tilde{\mathcal{J}}_h(u_h, z_h)\} < \infty$. By construction, the potential functions satisfy

$\tilde{\phi}_i(\mathbf{y}, \tilde{\mathbf{y}}) \geq \frac{\epsilon_\omega}{2} \|\mathbf{y}\|_2^2$, so for $C > 0$ we have

$$\begin{aligned} R_{\theta,h}(u_h) &= \lambda_\theta \sum_{i=1}^{N_C} \int_{\mathcal{T}_h \times \mathbb{T}} \tilde{\phi}_i(L_{h,i}[u_h](\mathbf{x}, t), \tilde{L}_{h,i}[u_h](\mathbf{x}, t)) d\Pi_h(\mathbf{x}, t) \\ &\geq \lambda_\theta \frac{\epsilon_\omega}{2} \sum_{i=1}^{N_C} \int_{\mathcal{T}_h \times \mathbb{T}} (\epsilon_\theta u_h(\mathbf{x}, t))^2 + |\nabla_{\Gamma_H}^h u_h(\mathbf{x}, t)|^2 + (K_{h,i}[u_h](\mathbf{x}, t))^2 d\Pi_h(\mathbf{x}, t) \\ &\geq C \int_{\mathcal{T}_h \times \mathbb{T}} (u_h(\mathbf{x}, t))^2 + |\nabla_{\Gamma_H}^h u_h(\mathbf{x}, t)|^2 d\Pi_h(\mathbf{x}, t) = C \|u_h\|_{\mathcal{V}_h}^2 \geq \tilde{C} \|u_h^l\|_{\mathcal{V}}^2. \end{aligned}$$

By weak compactness, any bounded sequence in the Hilbert space \mathcal{V} has a weakly convergent subsequence. Hence, there exists a subsequence $u_h^l \xrightarrow{\mathcal{V}} u^\infty$ and thus $u_h \xrightarrow{\mathcal{Z}} u^\infty$. By the liminf-inequality in Theorem 2, we know that

$$\mathcal{J}(u^\infty, z) \leq \liminf_{h \rightarrow 0} \tilde{\mathcal{J}}_h(u_h, z_h) = \liminf_{h \rightarrow 0} \inf_{v_h \in \mathcal{V}_h} \{ \tilde{\mathcal{J}}_h(v_h, z_h) \}.$$

The corresponding upper bound follows directly from the limsup-inequality of Theorem 2 by choosing a sequence $(\tilde{u}_h)_h$ converging to a minimizer of \mathcal{J}

$$\limsup_{h \rightarrow 0} \inf_{v_h \in \mathcal{V}_h} \{ \tilde{\mathcal{J}}_h(v_h, z_h) \} \leq \limsup_{h \rightarrow 0} \tilde{\mathcal{J}}_h(\tilde{u}_h, z_h) = \inf_{v \in \mathcal{V}} \{ \mathcal{J}(v, z) \}.$$

Finally, we conclude

$$\mathcal{J}(u^\infty, z) \leq \liminf_{h \rightarrow 0} \inf_{v_h \in \mathcal{V}_h} \{ \tilde{\mathcal{J}}_h(v_h, z_h) \} \leq \limsup_{h \rightarrow 0} \inf_{v_h \in \mathcal{V}_h} \tilde{\mathcal{J}}_h(v_h, z_h) \leq \inf_{v \in \mathcal{V}} \{ \mathcal{J}(v, z) \}$$

and therefore $u^\infty \in \arg \min_{v \in \mathcal{V}} \{ \mathcal{J}(v, z) \}$. \square

Remark 3. If R_θ is not assumed to be convex, then weak convergence in \mathcal{V} is no longer sufficient to pass to the limit in the liminf inequality. In this case, strong convergence in \mathcal{V} would be required. A natural approach to ensure this is to bound the minimizing sequence in a more regular space, for instance

$$H^1(\mathbb{T}; H^{-1}(\Gamma_H)) \cap L^2(\mathbb{T}; H^2(\Gamma_H)),$$

whose norm could be added to the energy functional with a small weight ($0 < \epsilon \ll 1$) to enforce additional regularity. By Aubin–Lions lemma, this space embeds compactly into \mathcal{V} , thereby guaranteeing strong convergence of minimizing sequences in \mathcal{V} .

5 Optimization

This section presents the variational formulation and numerical minimization of the inverse problem and Gaussian denoising, together with the bi-level optimization approach used to learn the regularizer.

5.1 Energy Minimization

We train the multivariate FoE-type regularizer on Gaussian-denoised functions in order to learn a data-driven prior that captures the structural properties of epicardial potentials. The learned regularizer functional is expected to generalize to other inverse problems beyond pure denoising. Let $v_h^m \in \mathcal{V}_h$, $m = 1, \dots, M$, denote noise-free inputs, scaled to the interval $[0, 1]$. The corresponding noisy observations are defined by

$$z_h^m = v_h^m + \kappa^m n_h^m, \quad m = 1, \dots, M,$$

where $n_h^m \in \mathcal{V}_h$ is a noise realization whose nodal coefficient vector satisfies $\mathbf{n}^m \sim \mathcal{N}(0, \mathbf{I}_{N_V \times (N_T+1)})$ and $\kappa^m > 0$ denotes the noise standard deviation. The proximal operator solves the denoising problem with regularizer $R_{\theta,h}$

$$\text{prox}(z_h) = \arg \min_{u_h \in \mathcal{V}_h} \left\{ \frac{1}{2} \|u_h - z_h\|_{\mathcal{Y}_h}^2 + R_{\theta,h}(u_h) \right\}. \quad (17)$$

In this formulation, Gaussian denoising corresponds to minimizing an energy functional of the same structure as in the inverse problem (3), except that the original data fidelity term $G(u, z)$ is replaced by $\tilde{G}(u, z) := \frac{1}{2} \|u - z\|_{\mathcal{Y}}^2$, which measures the squared L^2 -distance to the noisy input z . Both the inverse problem (3) and the denoising problem (17) are minimized using an accelerated gradient descent method with restart, as proposed in [7] and summarized in Algorithm 1. We first compute the Fréchet derivatives of the functions and then discretize them, representing them as vector-valued quantities using nodal values and matrix forms, as summarized in table 1. For the regularizer function R_θ , we restrict to only using the interpolated linear operators \tilde{L}_i for simplicity and define the linear operator $\tilde{L} : u \mapsto (\tilde{L}_1[u], \dots, \tilde{L}_{N_C}[u])$ and the vector valued derivative of the potential functions $\Phi(x_1, \dots, x_{N_C}) = (\phi'_1(x_1), \dots, \phi'_{N_C}(x_{N_C}))$ with

$$\phi'_i(\mathbf{y}) = \mu_i \left(\text{Proj}_{B_{\ell^1}}(\mathbf{y}/\mu_i) - \mathbf{Q}_i^\top \text{Proj}_{B_{\ell^1}}(\mathbf{Q}_i \mathbf{y}/(\mu_i \eta_i)) + \epsilon_\omega (\mathbf{I} - \mathbf{Q}_i^\top \mathbf{Q}_i) \mathbf{y} \right),$$

where $\|\mathbf{Q}_i\|_2 = 1$ ensures that ϕ'_i is Lipschitz continuous with constant $(1 + \epsilon_\omega)$. Furthermore, each linear operator \tilde{L}_i^* is discretized by

$$\tilde{L}_i^* \mathbf{u} = (\epsilon_\theta \mathbf{I}_{N_V \times (S+1)} + \sum_{j=1}^d \mathbf{M}^{-1} (\mathbf{P}^{\text{sp}} \nabla_{\Gamma_H, j})^\top \mathbf{M} + \mathbf{D}^{-1} (\mathbf{P}^{\text{temp}} \mathbf{K}_i)^\top \mathbf{D}) \mathbf{u}$$

to be adjoint in the finite element function spaces. The spatial and temporal mass matrices appear only in the components where the operator acts in space or time, respectively; if a component depends solely on space (resp. time), the corresponding temporal (resp. spatial) mass matrix does not appear. To determine the step size

Fréchet derivative	Discretization
$\mathcal{D}\tilde{G}(u, z)(\mathbf{x}, t) = (u - z)(\mathbf{x}, t)$	$\nabla \tilde{\mathbf{G}}_h(\mathbf{u}, \mathbf{z}) = \mathbf{u} - \mathbf{z}$
$\mathcal{D}G(u, z)(\mathbf{x}, t) = \tilde{A}^* \tilde{A}[u](\mathbf{x}, t) - \tilde{A}^*[z](\mathbf{x}, t)$	$\nabla \mathbf{G}_h(\mathbf{u}, \mathbf{z}) = \mathbf{M}^{-1} \tilde{\mathbf{A}}^\top (\tilde{\mathbf{A}} \mathbf{u} - \mathbf{z})$
$\mathcal{D}R_\theta(u)(\mathbf{x}, t) = \lambda_\theta \tilde{L}^* \Phi(\tilde{L}[u])(\mathbf{x}, t)$	$\nabla \mathbf{R}_{\theta,h}(\mathbf{u}) = \lambda_\theta \tilde{\mathbf{L}}^* \Phi(\tilde{\mathbf{L}} \mathbf{u})$

Table 1: Fréchet derivatives and their discrete approximations employed in optimization.

for Algorithm 1, we compute the Lipschitz constants of the derivatives. We estimate the largest eigenvalue of $\tilde{\mathbf{L}}^* \tilde{\mathbf{L}}$ via the power method:

$$\mathbf{u}_{k+1} = \frac{\tilde{\mathbf{L}}^* \tilde{\mathbf{L}} \mathbf{u}_k}{\|\tilde{\mathbf{L}}^* \tilde{\mathbf{L}} \mathbf{u}_k\|_2}, \quad \lambda_{\max}(\tilde{\mathbf{L}}^* \tilde{\mathbf{L}}) = \|\tilde{\mathbf{L}}^* \tilde{\mathbf{L}} \mathbf{u}_{N_{\lambda_{\max}}}\|_2,$$

with maximum iteration $N_{\lambda_{\max}} \in \mathbb{N}$. The Lipschitz constant of the derivative $\mathcal{D}(\tilde{G} + R_\theta)$ determines the step sizes in the accelerated gradient descent algorithm and is computed by $\mathcal{L} = 1 + (1 + \epsilon_\omega) \lambda_{\max}(\tilde{\mathbf{L}}^* \tilde{\mathbf{L}})$. When computing reconstructions to the inverse problem, the Lipschitz constant $\mathcal{D}G$ is computed by $\lambda_{\max}(\tilde{\mathbf{A}}^* \tilde{\mathbf{A}})$.

Algorithm 1: Accelerated gradient descent with objective-based restart

1. **Initialization:** Set $\mathbf{u}^0 = \mathbf{0}$, observation \mathbf{z} , Lipschitz constant \mathcal{L} of $\mathcal{D}(\tilde{\mathbf{G}} + R_\theta)$, $\tau_0 = 1$, $f^0 = \infty$, $\mathbf{v}^0 = \mathbf{u}^0$.

2. **Iteration** ($n \geq 0$): Compute

$$\begin{cases} \mathbf{u}^{n+1} = \mathbf{v}^n - \mathcal{L}^{-1} \nabla (\tilde{\mathbf{G}}_h(\mathbf{v}^n, \mathbf{z}) + \mathbf{R}_{\theta, h}(\mathbf{v}^n)), & \tau_{n+1} = \frac{1+\sqrt{1+4\tau_n^2}}{2}, \\ \mathbf{v}^{n+1} = \mathbf{u}^{n+1} + \frac{\tau_n-1}{\tau_{n+1}}(\mathbf{u}^{n+1} - \mathbf{u}^n), & f^{n+1} = \tilde{\mathbf{G}}_h(\mathbf{u}^n, \mathbf{z}) + \mathbf{R}_{\theta, h}(\mathbf{u}^n) \end{cases}$$

If $f^{n+1} > f^n$, reset: $\mathbf{v}^{n+1} = \mathbf{u}^{n+1}$, $\tau_{n+1} = 1$.

5.2 Learning the Regularizer

For regularizer generalization, we model R_θ as a function of the noise level κ via the weighting parameters $\mu_i(\kappa)$ in (7). Further details are provided in [7]. The regularizer is trained using the loss

$$\frac{1}{M} \sum_{m=1}^M \frac{1}{\sqrt{\kappa^m}} \|\mathbf{v}_h^m - \text{prox}_{R_{\theta, h}}(\mathbf{z}_h^m)\|_{\mathcal{Y}_h},$$

This results in a bi-level optimization problem: the inner problem optimizes $u_h \in \mathcal{V}_h$ by minimizing the energy, while the outer problem updates the parameters θ of the multivariate FoE regularizer (6). These parameters include the global weights λ_θ and ϵ_θ , the temporal kernel functions k_i , and the parameters of the potential functions ϕ_i , which are represented by a neural network. We compute the prior via denoising because the proximal operator of a regularizer effectively encodes the typical structure of noise-free functions: by learning R_θ such that $\text{prox}_{R_\theta}(\mathbf{z}_h)$ removes Gaussian noise, the regularizer captures the statistical properties of the clean functions \mathbf{v}_h^m . Once trained, the learned prior can be transferred to other inverse problems, providing robust guidance in situations where direct inversion is unstable.

For the optimization of the neural network parameters, we implement the model in PyTorch [23] and employ implicit differentiation to efficiently compute gradients through the equilibrium point defined by the model. Specifically, we use the `torchdeq` library [12], which provides scalable tools for deep equilibrium models, and adopt the Broyden algorithm as the fixed-point solver. This quasi-Newton method enables fast and memory-efficient convergence to the fixed point without requiring explicit backpropagation through all iterative solver steps. For optimizing the neural network parameters, we use the ADAM optimizer. The training is performed on an NVIDIA A40 GPU.

6 Results

We train and benchmark learned regularizer approaches for denoising and the inverse problem on 2D simulations, comparing them with state-of-the-art handcrafted finite element regularizers, including spatiotemporal first-order Tikhonov and TV.

6.1 Dataset Generation

We simulate 1000 epicardial potential fields on a 2D torso–heart model [11] illustrated in Figure 2, which includes the lungs. The data are randomly divided into 80% for training, 10% for validation, and 10% for testing. Synthetic data is generated by simulating cardiac activity on a finer 2D heart mesh with a finite element reaction–diffusion

model and interpolating to the coarser torso-heart model via nearest-neighbor interpolation to avoid inverse crimes. The transmembrane potential $v : \Omega_0 \times T \rightarrow \mathbb{R}$ is computed as proposed in [25]

$$C_m \partial_t v - \frac{1}{\beta} \nabla(\mathbf{G}_m \nabla v) + I_{\text{ion}}(v) = I_{\text{stim}}, \quad I_{\text{stim}}(\mathbf{x}, t) = \begin{cases} I_{\text{max}} \mathbf{1}_{\text{stim}}(\mathbf{x}), & 0 \leq t < I_{\text{dur}}, \\ 0, & t \geq I_{\text{dur}}, \end{cases}$$

with spatial indicator function for the randomly localised stimulus region $\mathbf{1}_{\text{stim}}$ and element-wise anisotropic intra- and extracellular conductivities \mathbf{G}_i and \mathbf{G}_e

$$\mathbf{G}_\alpha = \sigma_{\alpha,t} \mathbf{I} + (\sigma_{\alpha,l} - \sigma_{\alpha,t}) \mathbf{l} \otimes \mathbf{l}, \quad \alpha \in \{i, e\}, \quad \mathbf{G}_m = \mathbf{G}_i (\mathbf{G}_i + \mathbf{G}_e)^{-1} \mathbf{G}_e,$$

where \mathbf{l} is the local fiber direction, which in the heart model is taken to be circumferential around the ventricles, reflecting the typical orientation of myocardial fibers. The conductivities are computed following [26] by fixing $\sigma_{i,l}$ and determining the remaining components as functions of λ_{LT} , α , and ε :

$$\sigma_{i,t} = \frac{\sigma_{i,l}}{\lambda_{\text{LT}}^2} \left(\frac{1 + \alpha(1 - \varepsilon)}{1 + \alpha} \right), \quad \sigma_{e,t} = \frac{\sigma_{i,t}}{\alpha(1 - \varepsilon)}, \quad \sigma_{e,l} = \frac{\sigma_{i,l}}{\alpha}.$$

With probability 1/3, a randomly localized region of scar tissue with a prescribed radius is introduced by reducing the conductivity tensor \mathbf{G}_m by a factor drawn uniformly from [0.05, 0.25] and with probability 1/6, a second scar region is added. Ionic currents follow a Nagumo-type cubic model without repolarization,

$$I_{\text{ion}}(v) = g_{\text{max}}(v - V_{\text{rest}})(v - V_{\text{th}})(v - V_{\text{dep}}),$$

with fixed depolarization, resting, and threshold potentials. Time integration uses backward Euler with Δt , yielding

$$\left(C_m \mathbf{M} + \frac{\Delta t}{\beta} \mathbf{K}_m \right) \mathbf{v}^{n+1} = \mathbf{C} (C_m \mathbf{v}^n - \Delta t (I_{\text{ion}}(\mathbf{v}^n) - I_{\text{stim}})),$$

where \mathbf{K}_m corresponds to the finite element discretization of $\nabla \cdot (G_m \nabla \cdot)$, \mathbf{C} is the associated mass matrix, and \mathbf{v} contains the nodal values. The extracellular potential v_e is computed via the pseudo bidomain model [2] for each n_{sample} -th timestep

$$(\mathbf{K}_i + \mathbf{K}_e + \eta \mathbf{M}) \mathbf{v}_e = -\mathbf{K}_i \mathbf{v} \quad \text{with} \quad \eta = 10^{-9}.$$

Figure 3 illustrates a simulated epicardial potential that is part of the dataset, including scar tissue. The simulation parameters used to generate this dataset are summarized in Table 2.

V_{rest}	V_{dep}	V_{th}	g_{max}	$\sigma_{i,l}$	λ_{LT} [26]	ε [26]
-85mV	30mV	-55mV	1.4×10^{-3}	3S/m	[2.16, 2.84]	[0.58, 0.93]
α [26]	C_m [25]	β [25]	I_{max}	I_{dur}	Δt	n_{sample}
1	$1\mu\text{F}/\text{cm}^2$	100cm^{-1}	$1.2\mu\text{A}/\text{cm}^2$	100ms	[0.07, 0.12]ms	[7, 13]

Table 2: Model parameters and sampling ranges used for the generation of the synthetic dataset. Parameters are drawn uniformly at random from the indicated intervals.

6.2 Baseline Methods

As handcrafted baselines, we consider spatiotemporal first-order Tikhonov (**TIK**) regularization,

$$\tilde{G}(u, z) + \frac{1}{2} \|\Lambda \nabla_{(\mathbf{x}, t)} u\|_{\mathcal{Y}^d}^2,$$

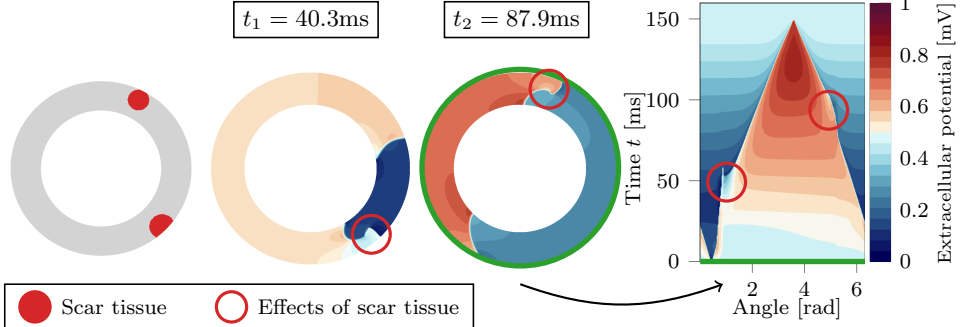


Figure 3: Extracellular potential v on the myocardium at three time steps with scar tissue, and a spacetime plot on the epicardium normalized to $[0, 1]$. Reduced conductivity in the scar region deforms the characteristic spike-shaped potentials and slows propagation.

where $\Lambda = \text{diag}(\lambda_\gamma, \dots, \lambda_\gamma, \lambda_t) \in \mathbb{R}_+^{(d+1) \times (d+1)}$, and λ_γ and λ_t denote the spatial and temporal regularization parameters, respectively. The optimization problem is solved by applying the conjugate gradient method to the optimality system. In addition, we compare against isotropic spatiotemporal total variation (**TV**) regularization [15],

$$\tilde{G}(u, z) + \int_{\Gamma_H \times \mathbb{T}} \|\Lambda \nabla_{(\mathbf{x}, t)} u(\mathbf{x}, t)\|_2 \, d\Pi(\mathbf{x}, t),$$

which is minimized using a first-order primal–dual algorithm. All baseline methods are computed using lumped mass matrices, as this significantly reduces computation time while producing visually and L^2 -error-wise negligible differences.

6.3 Denoising

We first evaluate the FoE models on Gaussian denoising of epicardial potentials, where the ground truth (**GT**) functions are corrupted with Gaussian noise of standard deviation κ , matching the noise used during training. This section highlights the model’s ability to reconstruct clean signals from noisy observations, motivating their use as priors for more general inverse problems. Finally, we evaluate the proposed spatiotemporal FoE–type regularizer in both a convex (**CMFoE**) and a non-convex (**MFoE**) formulation. The convex version ensures theoretical guarantees and predictable behavior, while the non-convex version offers greater flexibility to capture complex signal correlations and potentially improve empirical performance. The parameters used for tuning the models are the input noise level κ and the learned weighting parameter λ_θ . To increase the range of the filters, we compute each filter as a composition of three filters defined on a smaller interval, increasing the number of output channels for each cross-correlation, i.e. $k_i(t) = \int_{\mathbb{R}^2} k_i^3(s) k_i^2(\tau) k_i^1(\tau + s + t) d(s, \tau)$ for $k_i^j \in L^1(\tilde{\mathbb{T}})$ and $k_i^j = 0$ on $\mathbb{R} \setminus \tilde{\mathbb{T}}$. The piecewise affine kernel functions k_{h_i} learned from Gaussian denoising, with each $k_{h_i}^j$ defined on $\tilde{\mathbb{T}} = [t_{-2}, t_2]$ are shown in Figure 4. The models are trained for 10000 iterations with a learning rate of 0.005 decaying by 0.75 after 2500 iterations and a batch size of 1 due to the varying number of temporal values of the nodal vectors.

Figure 5 illustrates representative denoising results obtained with the different regularization approaches for noise level $\kappa = 0.2$. In Table 3, errors for denoising across multiple different noise levels on the test set are computed by tuning the parameters on the validation set first. As expected, **TIK** regularization produces overly smooth reconstructions: while it effectively reduces noise, it also blurs sharp features and fails to preserve edges, resulting in a loss of fine structural details. In

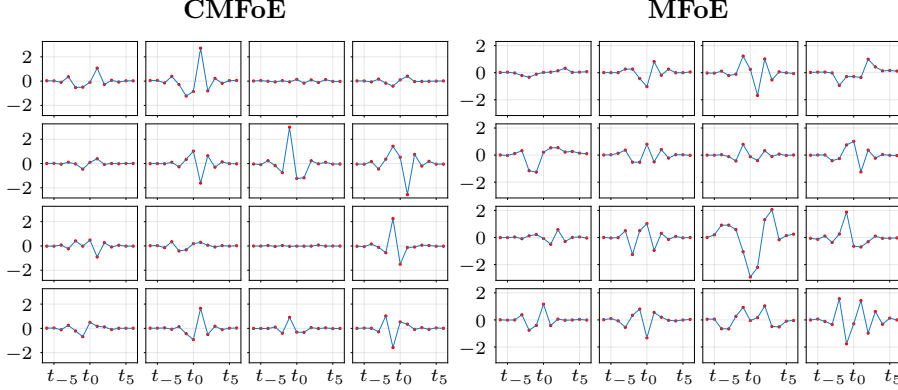


Figure 4: Learned kernel functions $(k_{h,i})_{i=1}^{N_C}$ for $N_C = 16$ of the FoE approaches by denoising.

contrast, **TV** regularization yields reconstructions with significantly sharper edges. Discontinuities and piecewise constant regions are well preserved. The spatiotemporal **CMFoE** and **MFoE** regularizers yield the best denoising performance with significant improvement for the nonconvex case, effectively suppressing Gaussian noise while preserving sharp spatial and temporal features. Its learned filters adapt better to the noise characteristics than handcrafted regularizers, producing reconstructions that are visually and quantitatively closer to the ground truth.

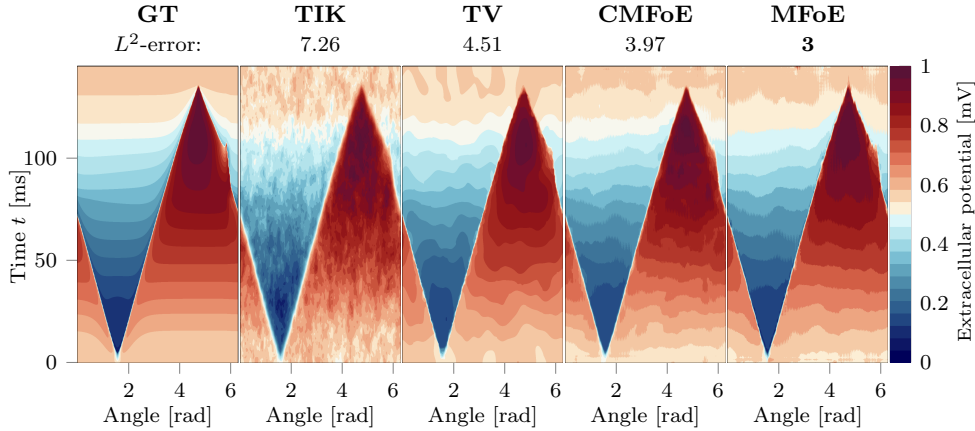


Figure 5: Denoising reconstructions and L^2 -errors of multiple regularization approaches for an observation with a noise level of $\kappa = 0.2$ applied on the ground truth visualized in a space-time plot.

6.4 Inverse Problem

We next consider the inverse problem in electrocardiographic imaging, again comparing **TIK** regularization, **TV** regularization, and the proposed spatiotemporal **CMFoE** and **MFoE** approaches as illustrated in fig. 6 and evaluated for different noise levels measured in signal-to-noise ratio (SNR) of the observations in table 4. In contrast to the pure denoising setting, the inverse problem is severely ill-posed, and the reconstructions require substantially longer computation times due to the repeated solution of forward and adjoint problems within the optimization procedure. The ill-posedness of the inverse problem is clearly reflected in the reconstruction

κ \ Reg.	TIK	TV	CMFoE	MFoE
0.05	3.85	2.16	1.72	1.59
	$\lambda_\gamma, \lambda_t = 0.595, 1.189$	$\lambda_\gamma, \lambda_t = 0.088, 0.044$	$\lambda_\theta, \kappa = 6.97, 0.02$	$\lambda_\theta, \kappa = 7.23, 0.05$
0.1	5.4	3.15	2.6	2.19
	$\lambda_\gamma, \lambda_t = 1.091, 1.834$	$\lambda_\gamma, \lambda_t = 0.177, 0.088$	$\lambda_\theta, \kappa = 6.97, 0.1$	$\lambda_\theta, \kappa = 7.23, 0.1$
0.2	7.32	4.74	3.84	3.23
	$\lambda_\gamma, \lambda_t = 1.834, 2.828$	$\lambda_\gamma, \lambda_t = 0.354, 0.177$	$\lambda_\theta, \kappa = 6.97, 0.2$	$\lambda_\theta, \kappa = 7.23, 0.2$

Table 3: Mean L^2 -errors and corresponding regularization parameters for denoising reconstructions of different noise levels with standard deviation $\kappa \in (0.05, 0.1, 0.2)$.

quality. **TV** regularization improves edge preservation and produces sharper spatial features, but may introduce artificial discontinuities, especially in regions with low signal-to-noise ratio. The **MFoE** regularizer again provides the best overall performance. Despite the increased difficulty of the inverse problem, it is able to capture relevant spatiotemporal activation patterns more accurately and to suppress noise and inversion artifacts more effectively than the classical approaches. In particular, the learned temporal interactions help stabilize the reconstruction and reduce non-physical oscillations over time. Importantly, although the inverse problem is more challenging than in the denoising case, the ranking of the regularizers in terms of performance remains the same.

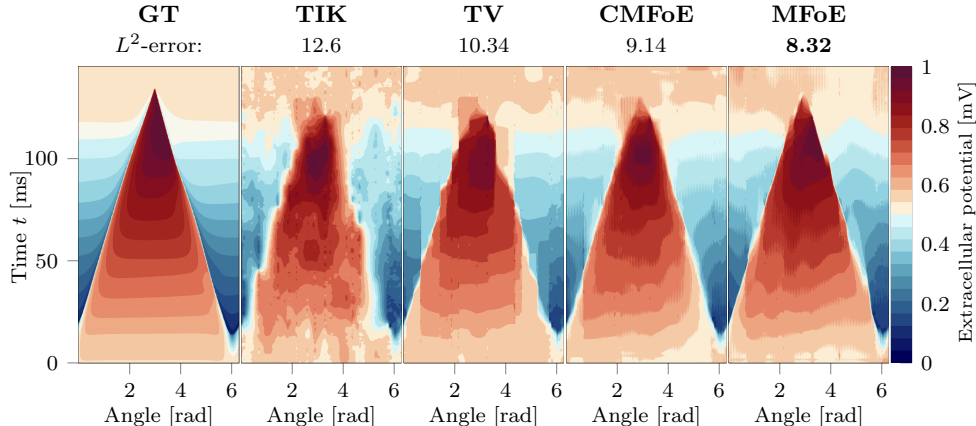


Figure 6: Inverse problem reconstructions and L^2 -errors of multiple regularization approaches with SNR of 30 dB by applying Gaussian noise on the observations, visualized in a space-time plot.

7 Conclusion

We introduced a class of trained spatiotemporal regularizers for inverse problems on unstructured meshes and analyzed them within a rigorous variational framework. We proved theoretical Mosco-convergence of the discrete functionals to their continuous limits, which implies convergence of minimizers and ensures stability under mesh refinement. Numerical experiments on denoising and the inverse problem show that the proposed spatiotemporal regularizer consistently outperforms classical handcrafted approaches. Although the inverse problem is severely ill-posed and reconstructions require longer computation times, the relative performance of the regularizers in contrast to each other remains unchanged. The current implementation is limited to uniform timesteps, which restricts its applicability in problems

Reg. SNR \	TIK	TV	CMFoE	MFoE
50	12.82	9.19	8.09	7.59
	$\lambda_\gamma = 2.97 \times 10^{-3}$ $\lambda_t = 2.97 \times 10^{-3}$	$\lambda_\gamma = 4.59 \times 10^{-6}$ $\lambda_t = 9.64 \times 10^{-7}$	$\lambda_\theta = 6.97 \times 10^{-3}$ $\kappa = 8.84 \times 10^{-2}$	$\lambda_\theta = 9.04 \times 10^{-4}$ $\kappa = 4.2 \times 10^{-1}$
40	13.01	9.98	9.02	8.11
	$\lambda_\gamma = 8.41 \times 10^{-3}$ $\lambda_t = 8.41 \times 10^{-3}$	$\lambda_\gamma = 2.83 \times 10^{-5}$ $\lambda_t = 5.95 \times 10^{-6}$	$\lambda_\theta = 3.49 \times 10^{-2}$ $\kappa = 8.84 \times 10^{-2}$	$\lambda_\theta = 5.11 \times 10^{-3}$ $\kappa = 4.2 \times 10^{-1}$
30	13.54	11.72	10.74	10.48
	$\lambda_\gamma = 2.38 \times 10^{-2}$ $\lambda_t = 2.38 \times 10^{-2}$	$\lambda_\gamma = 2 \times 10^{-4}$ $\lambda_t = 4.59 \times 10^{-5}$	$\lambda_\theta = 8.29 \times 10^{-1}$ $\kappa = 2.87 \times 10^{-2}$	$\lambda_\theta = 1.81 \times 10^{-2}$ $\kappa = 5 \times 10^{-1}$

Table 4: Mean L^2 -errors and corresponding regularization parameters for inverse problem reconstructions at SNR (30, 40, 50) dB.

requiring adaptive or variable temporal resolution. Extending the method to variable timesteps would increase computational complexity. Similarly, extending the model to learn kernel convolutions on spatial manifolds, analogous to temporal convolutions, is computationally demanding, thereby limiting the practicality of spatial regularization. Overall, this work shows that data-driven regularization can be combined with strong analytical guarantees, yielding methods that are both theoretically sound and practically superior for challenging inverse problems such as ECGI.

References

- [1] F. B. BELGACEM, *Why is the Cauchy problem severely ill-posed?*, Inverse Problems, 23 (2007), pp. 823–836, <https://doi.org/10.1088/0266-5611/23/2/020>, <https://doi.org/10.1088/0266-5611/23/2/020>.
- [2] M. J. BISHOP AND G. PLANK, *Bidomain ECG Simulations Using an Augmented Monodomain Model for the Cardiac Source*, IEEE transactions on bio-medical engineering, 58 (2011), p. 10.1109/TBME.2011.2148718, <https://doi.org/10.1109/TBME.2011.2148718>, <https://www.ncbi.nlm.nih.gov/pmc/articles/PMC3378475/> (accessed 2022-07-19).
- [3] S. C. BRENNER AND L. R. SCOTT, *The mathematical theory of finite element methods*, vol. 15 of Texts in Applied Mathematics, Springer, New York, third ed., 2008, <https://doi.org/10.1007/978-0-387-75934-0>, <https://doi.org/10.1007/978-0-387-75934-0>.
- [4] P. G. CIARLET, *The finite element method for elliptic problems*, vol. Vol. 4 of Studies in Mathematics and its Applications, North-Holland Publishing Co., Amsterdam-New York-Oxford, 1978.
- [5] M. CLUITMANS, D. H. BROOKS, R. MACLEOD, O. DÖSSEL, M. S. GUILLEM, P. M. VAN DAM, J. SVEHLIKOVA, B. HE, J. SAPP, L. WANG, AND L. BEAR, *Validation and opportunities of electrocardiographic imaging: From technical achievements to clinical applications*, Frontiers in Physiology, 9 (2018), <https://doi.org/10.3389/fphys.2018.01305>, <https://www.frontiersin.org/articles/10.3389/fphys.2018.01305>.
- [6] P. COLLI FRANZONE, L. F. PAVARINO, AND S. SCACCHI, *Mathematical cardiac electrophysiology*, vol. 13 of MS&A. Modeling, Simulation and Applications, Springer, Cham, 2014, <https://doi.org/10.1007/978-3-319-04801-7>, <https://doi.org/10.1007/978-3-319-04801-7>.
- [7] S. DUCOTTERD AND M. UNSER, *Multivariate fields of experts*, 2025, <https://arxiv.org/abs/2508.06490>, <https://arxiv.org/abs/2508.06490>.

- [8] A. EFLAND, S. NEUMAYER, AND M. RUMPF, *Convergence of the time discrete metamorphosis model on Hadamard manifolds*, SIAM J. Imaging Sci., 13 (2020), pp. 557–588, <https://doi.org/10.1137/19M1247073>, <https://doi.org/10.1137/19M1247073>.
- [9] C. M. ELLIOTT AND T. RANNER, *Finite element analysis for a coupled bulk-surface partial differential equation*, IMA J. Numer. Anal., 33 (2013), pp. 377–402, <https://doi.org/10.1093/imanum/drs022>, <https://doi.org/10.1093/imanum/drs022>.
- [10] L. C. EVANS, *Partial differential equations*, vol. 19 of Graduate Studies in Mathematics, American Mathematical Society, Providence, RI, 1998, <https://doi.org/10.1090/gsm/019>, <https://doi.org/10.1090/gsm/019>.
- [11] L. GANDER, R. KRAUSE, M. MULTERER, AND S. PEZZUTO, *Space-time shape uncertainty in the forward and inverse problem of electrocardiography*, International Journal for Numerical Methods in Biomedical Engineering, 37 (2021), <https://doi.org/10.1002/cnm.3522>, <https://arxiv.org/abs/2010.16104>.
- [12] Z. GENG AND J. Z. KOLTER, *Torchdeq: A library for deep equilibrium models*, <https://github.com/locuslab/torchdeq>, 2023.
- [13] A. GOUJON, S. NEUMAYER, AND M. UNSER, *Learning weakly convex regularizers for convergent image-reconstruction algorithms*, SIAM J. Imaging Sci., 17 (2024), pp. 91–115, <https://doi.org/10.1137/23M1565243>, <https://doi.org/10.1137/23M1565243>.
- [14] T. GRANDITS, J. VERHÜLDONK, G. HAASE, A. EFLAND, AND S. PEZZUTO, *Digital twinning of cardiac electrophysiology models from the surface ECG: a geodesic backpropagation approach*, IEEE Transactions on Biomedical Engineering, 71 (2024), pp. 1281–1288, <https://doi.org/10.1109/TBME.2023.3331876>, <https://arxiv.org/abs/2308.08410>.
- [15] M. HAAS, T. GRANDITS, T. PINETZ, T. BEIERT, S. PEZZUTO, AND A. EFLAND, *Finite Element-Based Space-Time Total-Variation-Type Regularization of the Inverse Problem in Electrocardiographic Imaging*, SIAM J. Sci. Comput., 47 (2025), pp. B1317–B1342, <https://doi.org/10.1137/24M1685055>, <https://doi.org/10.1137/24M1685055>.
- [16] E. HEBEY, *Sobolev spaces on Riemannian manifolds*, vol. 1635 of Lecture Notes in Mathematics, Springer-Verlag, Berlin, 1996, <https://doi.org/10.1007/BFb0092907>, <https://doi.org/10.1007/BFb0092907>.
- [17] A. KAROUI, L. BEAR, P. MIGERDITCHIAN, AND N. ZEMZEMI, *Evaluation of fifteen algorithms for the resolution of the electrocardiography imaging inverse problem using ex-vivo and in-silico data*, Frontiers in Physiology, 9 (2018), <https://doi.org/10.3389/fphys.2018.01708>.
- [18] E. KOBLER, A. EFLAND, K. KUNISCH, AND T. POCK, *Total deep variation: A stable regularization method for inverse problems*, IEEE Transactions on Pattern Analysis and Machine Intelligence, 44 (2022), pp. 9163–9180, <https://doi.org/10.1109/TPAMI.2021.3124086>.
- [19] J. MOREAU, *Proximité et dualité dans un espace hilbertien*, Bulletin de la Société Mathématique de France, 93 (1965), pp. 273–299, <http://eudml.org/doc/87067>.
- [20] U. MOSCO, *Convergence of convex sets and of solutions of variational inequalities*, Advances in Math., 3 (1969), pp. 510–585, [https://doi.org/10.1016/0001-8708\(69\)90009-7](https://doi.org/10.1016/0001-8708(69)90009-7), [https://doi.org/10.1016/0001-8708\(69\)90009-7](https://doi.org/10.1016/0001-8708(69)90009-7).

[21] G. NARDI, B. CHARLIER, AND A. TROUVÉ, *The matching problem between functional shapes via a BV penalty term: a Γ -convergence result*, Interfaces Free Bound., 26 (2024), pp. 381–414, <https://doi.org/10.4171/ifb/517>, <https://doi.org/10.4171/ifb/517>.

[22] M. ONAL AND Y. SERINAGAOGLU, *Spatio-temporal solutions in inverse electrocardiography*, in 4th European Conference of the International Federation for Medical and Biological Engineering, J. Vander Sloten, P. Verdonck, M. Nyssen, and J. Haueisen, eds., Berlin, Heidelberg, 2009, Springer Berlin Heidelberg, pp. 180–183.

[23] A. PASZKE, S. GROSS, F. MASSA, A. LERER, J. BRADBURY, G. CHANAN, T. KILLEEN, Z. LIN, N. GIMELSHEIN, L. ANTIGA, A. DESMAISON, A. KÖPF, E. YANG, Z. DEVITO, M. RAISON, A. TEJANI, S. CHILAMKURTHY, B. STEINER, L. FANG, J. BAI, AND S. CHINTALA, *PyTorch: an imperative style, high-performance deep learning library*, Curran Associates Inc., Red Hook, NY, USA, 2019.

[24] S. PEZZUTO, P. PERDIKARIS, AND F. SAHLI COSTABAL, *Learning cardiac activation maps from 12-lead ECG with multi-fidelity Bayesian optimization on manifolds*, IFAC-PapersOnLine, 55 (2022), pp. 175–180, <https://doi.org/10.1016/j.ifacol.2022.09.091>, <https://arxiv.org/abs/2203.06222>.

[25] M. POTSE, B. DUBE, J. RICHER, A. VINET, AND R. M. GULRAJANI, *A comparison of monodomain and bidomain reaction-diffusion models for action potential propagation in the human heart*, IEEE Transactions on Biomedical Engineering, 53 (2006), pp. 2425–2435, <https://doi.org/10.1109/TBME.2006.880875>.

[26] B. J. ROTH, *Electrical conductivity values used with the bidomain model of cardiac tissue*, IEEE Transactions on Biomedical Engineering, 44 (2002), pp. 326–328.

[27] S. ROTH AND M. J. BLACK, *Fields of experts: a framework for learning image priors*, 2005 IEEE Computer Society Conference on Computer Vision and Pattern Recognition (CVPR’05), 2 (2005), pp. 860–867 vol. 2, <https://api.semanticscholar.org/CorpusID:2843211>.

[28] L. I. RUDIN, S. OSHER, AND E. FATEMI, *Nonlinear total variation based noise removal algorithms*, Physica D: Nonlinear Phenomena, 60 (1992), pp. 259–268, [https://doi.org/https://doi.org/10.1016/0167-2789\(92\)90242-F](https://doi.org/https://doi.org/10.1016/0167-2789(92)90242-F), <https://www.sciencedirect.com/science/article/pii/016727899290242F>.

[29] M. SEGER, G. FISCHER, R. MODRE-OSPRIAN, B. MESSNARZ, F. HANSER, AND B. TILG, *Lead field computation for the electrocardiographic inverse problem - finite elements versus boundary elements*, Computer methods and programs in biomedicine, 77 (2005), pp. 241–52, <https://doi.org/10.1016/j.cmpb.2004.10.005>.

[30] R. TENDERINI, S. PAGANI, A. QUARTERONI, AND S. DEPARIS, *PDE-aware deep learning for inverse problems in cardiac electrophysiology*, SIAM J. Sci. Comput., 44 (2022), pp. B605–B639, <https://doi.org/10.1137/21M1438529>, <https://doi.org/10.1137/21M1438529>.

[31] A. N. TIKHONOV AND V. Y. ARSENIN, *Solutions of ill-posed problems*, Scripta Series in Mathematics, V. H. Winston & Sons, Washington, DC; John Wiley & Sons, New York-Toronto-London, 1977. Translated from the Russian, Preface by translation editor Fritz John.

[32] D. WANG, R. M. KIRBY, AND C. R. JOHNSON, *Resolution strategies for the finite-element-based solution of the ecg inverse problem*, IEEE Transactions on Biomedical Engineering, 57 (2010), pp. 220–237, <https://doi.org/10.1109/TBME.2009.2024928>.